

---

# CAN AI WEATHER MODELS PREDICT BEYOND TWO WEEKS? A QUANTITATIVE BENCHMARK AND ANALYSIS OF LONG ROLLOUTS

---

**Fanny Lehmann**  
 ETH AI Center  
 ETH Zurich  
 fanny.lehmann@ai.ethz.ch

**Firat Ozdemir**  
 Swiss Data Science Center  
 ETH Zurich & EPFL

**Yun Cheng**  
 Swiss Data Science Center  
 ETH Zurich & EPFL

**Torsten Hoefler**  
 Scalable Parallel Computing Lab  
 ETH Zurich

**Sebastian Schemm**  
 Dep. of Applied Mathematics and Theoretical Physics  
 University of Cambridge

**Benedikt Soja**  
 Institute of Geodesy and Photogrammetry  
 ETH Zurich

**Siddhartha Mishra**  
 Seminar for Applied Mathematics  
 ETH Zurich

## ABSTRACT

While AI weather models excel at short-to-medium range forecasts (up to 15 days), they frequently suffer from ill-defined “instabilities” when rolled out over longer horizons. This work addresses the lack of a formal taxonomy by categorizing these failures into three distinct regimes — blow-up, drift, and loss of seasonality — through year-long rollouts of nine state-of-the-art AI weather models. Our analysis reveals that stability hinges on the treatment of small spatio-temporal scales: unstable models amplify high-frequency energy, while stable models act as denoisers when noise is added to their inputs. Far from reducing these models to mere stochastic *parrots*, our findings highlight that stable models generate unique weather trajectories, conditioned on the initial state. We verify our findings through ablation studies on architectural design choices, conducted using state-of-the-art Vision Transformer (ViT) AI weather model architectures.

## 1 Introduction

AI weather models have surpassed numerical solvers on standard metrics at weather time scales (up to 15 days), but producing realistic predictions over longer horizons remains a fundamental challenge. A common approach for long-term prediction applies the model autoregressively, feeding its own output back as input at each step. This yields rollouts of arbitrary length, but predictions frequently *blow up* or become unrealistically blurry as the number of autoregressive steps grows, and no formal characterization of these failure modes exists [5, 4].

While long-term stability remains elusive for many AI weather models, recent climate-scale emulators demonstrate remarkable autoregressive robustness, an effect that appears architecture-agnostic. Success has been observed across a variety of backbone architectures, including Spherical Fourier Neural Operators (ACE2 [29], LUCIE [14]), UNet Convolutional Neural Networks (DLESyM [11]), and 3D Swin Transformers (ArchesWeather [10]). Typically, the

main difference between AI weather models and AI climate emulators is the spatio-temporal resolution of the data with which they are trained and operate. While most state-of-the-art weather models operate at a spatial resolution of  $0.25^\circ$  and temporal resolution of 6 hours, climate emulators lower the spatial resolution to  $1.0^\circ$ , at best (see Table A.1) and sometimes increase the lead time to one day or more. This work investigates the influence of spatio-temporal resolution on long-term stability as a potential explanation for the success of climate emulators on decadal timescales.

Prior work has proposed several hypotheses to explain long-rollout instability. Some works suggest that models need to account for the spherical structure of the Earth to correctly represent all spatial scales, using spherical harmonics or HEALPix meshes for this purpose [5, 16]. Chattopadhyay et al. identify spectral bias as the root cause of instability [8]. They propose a new framework (FouRKS) for spectral regularization but only demonstrate its benefits on low-resolution data ( $2^\circ$  and 24h lead time), leaving it unclear whether these benefits generalize to the high-resolution ( $0.25^\circ$ ) regimes common to state-of-the-art AI weather models.

AI Earth system models are increasingly positioned as tools for studying climate change, given their demonstrated ability to reproduce atmospheric dynamics. Beyond the physical constraints required to design meaningful climate emulators, a prerequisite for any climate application is that models sustain long rollouts without unphysical drift, blow-up, or spectral artifacts. This work supports active efforts in the AI for Weather and Climate community to address time scales longer than weather, such as the Weather Quest targeting subseasonal to seasonal timescales [22] and the AI4MIP experiment focusing on climatic time scales.

## 2 Related Work

Several AI models achieve decadal stability: ACE2 sustains rollouts up to 81 years [29] and NeuralGCM up to 40 years [17]. However, this stability is not unconditional: ACE2 required selecting specific checkpoints, and NeuralGCM yielded stable 40-year rollouts for only 22 of 37 tested initial conditions [17]. The Triton model achieves 1-year stability through a multi-grid architecture that addresses spectral bias [31], but its predictions exhibit significant smoothing after several months, degrading physical realism. Challenges related to long-term stability have already been raised but only described visually [8] or at a low spatial resolution [12]. McCabe et al. give an in-depth analysis of stability failure modes in FNO and propose several architectural changes related to spectral convolutions that improved stability up to 400 rollout steps [23].

Outside of the weather domain, several approaches have been proposed to stabilize autoregressive models. Multi-step loss functions improve long-term stability but are memory-prohibitive for large models, motivating backpropagation through only the final rollout step [7, 34]. Instability often arises when autoregressive predictions drift out of the training distribution. Robustness can be improved by injecting noise during rollout [21], denoising predictions via diffusion models as in Thermalizer [26], or adding regularization terms such as a Jacobian penalty to the loss function [24]. Finally, Armegioiu highlights the influence of unresolved variables on rollout stability for generative models and shows the benefits of keeping a memory of the physical system to stabilize rollouts [1].

## 3 A Taxonomy of Rollout Instabilities

We analyze nine state-of-the-art weather models spanning model sizes from 3.5M to 4.7B parameters and four architecture families (see Table A.1). For each model, we run a 2-year rollout (2,920 autoregressive steps at 6-hour lead time), initialized on January 1, 2021 — outside the training period of all models except AIFS (due to sea surface temperature forcing availability for some models). The ERA5 reanalysis [15] serves as reference data since all models are trained on the ERA5 dataset.

Figure 1 shows 2-meter temperature time series over the Arctic, a particularly sensitive diagnostic region where spherical geometry compresses grid spacing at high latitudes, often causing instabilities to manifest there before propagating to lower latitudes. Figure 1 reveals markedly different behavior across models: Aurora, SFNO, and DLESyM track the ERA5 seasonal cycle closely throughout, while the minimum temperature predicted by AIFS, FourCastNet, and FuXi diverges rapidly from ERA5.

Beyond visual inspection, we introduce quantitative metrics that systematically characterize rollout behavior across variables and spatial scales. Although results are presented for one rollout, Tables A.2 and A.3 show that metrics are robust to different initialization dates.

**The blow-up time** is defined as the onset of unbounded exponential growth in spatial extremes. Specifically, we identify the first 30-day window where the global minimum or maximum value yields a high log-linear correlation, signifying a transition from physical oscillation to numerical divergence (Appendix B.1). Table 1 extends the observations from Fig. 1 by showing that Aurora, SFNO, Pangu, and DLESyM do not blow-up for any of the nine variables throughout

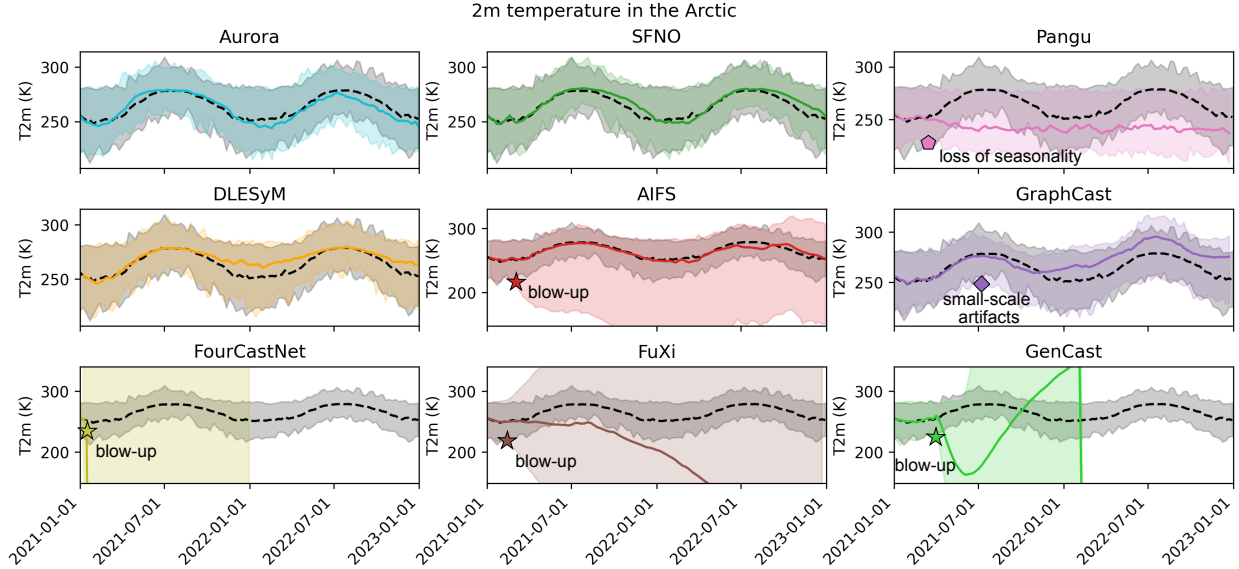


Figure 1: Rollouts initialized on January 1st, 2021 for nine AI weather models. The lines show 2-meter temperature averaged across the Arctic for the reference ERA5 (black) and the model (color). The shaded areas extend from the minimum to the maximum temperature over the Arctic for ERA5 (grey) and the model (color). FourCastNet and GenCast results are shown only until they reach unphysical values.

Table 1: Number of days until the model predictions blow-up, defined as an exponential growth of the spatial extremes (see Appendix B.1 for details). “-” denotes variables absent from the models.

Model	T2m	U10m	MSLP	Z500	T500	Q500	U300	T100	Q100
Aurora	> 730	> 730	> 730	> 730	> 730	> 730	> 730	> 730	> 730
SFNO	> 730	> 730	> 730	> 730	> 730	> 730	> 730	> 730	> 730
Pangu	> 730	> 730	> 730	> 730	> 730	> 730	> 730	> 730	> 730
AIFS	41	> 730	> 730	16	> 730	> 730	> 730	> 730	416
GraphCast	360	379	287	274	344	470	289	457	352
FourCastNet	8	8	8	9	-	-	-	-	-
FuXi	431	10	> 725	491	444	-	82	402	-
DLESyM	> 730	-	-	> 730	-	-	-	-	-
GenCast	76	> 725	76	71	77	> 725	> 725	91	217

our study over different pressure levels. AIFS behavior is inconsistent across variables and we noticed earlier blow-up with the probabilistic AIFS-CRPS [20] (Fig. A.3).

**Seasonality** is quantified from the energy spectra averaged over wavelengths larger than 5000 km as seasonal fluctuations affect large spatial scales. A model is deemed to lose seasonality when its large-scale energy spectrum deviates from ERA5 by more than twice the climatological range for at least 45 consecutive days (Appendix B.2). This definition confirms that Pangu rollouts lose seasonality and collapse to a time-invariant global state (Table 2 and Fig. A.1), likely because Pangu lacks a time embedding and therefore has no access to long-term temporal information. Although counter-intuitive, AIFS and GraphCast can preserve seasonality while blowing up (Fig. A.2): blow-up manifests locally, whereas seasonality is computed from large-scale spectral coefficients that are insensitive to spatially limited effects. Top-of-atmosphere specific humidity is the only case where we observed stability failure modes for Aurora and SFNO (Fig. A.2).

**The small spatial scales** exhibit one of three distinct behaviors throughout long rollouts: (i) they are smoothed out and forecasts become blurry, (ii) they preserve realistic sharpness compared to the reference, (iii) they get amplified and lead to unrealistic small-scale artifacts. The small-scale energy spectra (wavelengths smaller than 250 km) are used to quantify these trends by comparing the mean small-scale spectra during the last 30 days of the rollout with the mean ERA5 spectra over the same period (Appendix B.3). Table 3 shows ratios less than 1 for Aurora, SFNO, Pangu, and DLESyM, indicating that the predictions tend to be blurrier than the ERA5 reference. However, the blurriness

Table 2: Number of days until loss of seasonality, defined as the energy spectra of large wavelengths exceeding climatology for at least 45 days (see Appendix B.2 for details)

Model	T2m	U10m	MSLP	Z500	T500	Q500	U300	T100	Q100
Aurora	> 730	> 730	> 730	> 730	> 730	> 730	> 730	> 730	> 730
SFNO	> 730	> 730	> 730	> 730	> 730	> 730	> 730	> 730	> 730
Pangu	181	> 730	> 730	> 730	525	202	> 730	> 730	282
AIFS	599	463	499	590	504	473	475	498	377
GraphCast	228	318	> 725	> 725	600	167	382	176	107
FourCastNet	60	61	64	62	-	-	-	-	-
FuXi	185	56	280	243	207	-	100	323	-
DLESyM	> 730	-	-	> 730	-	-	-	-	-
GenCast	96	97	102	105	91	105	94	83	79

Table 3: Ratio between the predicted and reference small-scale energy spectra at the end of the rollout. Numbers in parentheses indicate the ratio between energy spectra at the end and beginning of the prediction rollout (see Appendix B.3 for details). The optimal value is 1; values less than 1 indicate smooth predictions while values greater than 1 indicate increased small-scale energy.

Model	T2m	U10m	MSLP	Z500	T500	Q500	U300	T100	Q100
Aurora	0.8 (1.0)	0.6 (0.8)	0.8 (0.8)	2.3 (0.8)	0.3 (0.6)	0.1 (0.4)	0.2 (0.6)	1.0 (1.9)	1.0 (3.5)
SFNO	0.8 (1.1)	0.5 (0.9)	1.0 (1.1)	5.6 (6.1)	0.5 (1.6)	0.1 (0.3)	0.1 (0.4)	1.0 (2.2)	0.9 (0.9)
Pangu	0.7 (0.9)	0.3 (0.7)	0.6 (0.6)	1.2 (1.3)	0.3 (0.7)	0.02 (0.1)	0.2 (0.4)	0.6 (1.1)	0.9 (2.5)
AIFS	0.6 (1.1)	1.0 (2.3)	12 (21)	3.9 (5.6)	8.1 (71)	0.2 (3.2)	0.6 (5.1)	9.7 (95)	0.7 (11)
GraphCast	3.7 (4.4)	0.8 (0.9)	5.5 (4.8)	3e2 (1e2)	80 (1e2)	3.2 (20)	0.7 (1.1)	2e2 (4e2)	1.0 (4.7)
FourCastNet	9e5 (1e6)	1e5 (2e5)	1.0 (1.0)	7.4 (1.0)	-	-	-	-	-
FuXi	2e3 (2e3)	0.7 (1.0)	2e4 (3e4)	3e5 (2e5)	1e5 (1e5)	-	3e2 (4e2)	2e5 (3e5)	-
DLESyM	0.03 (1.0)	-	-	0.1 (0.8)	-	-	-	-	-
GenCast	1.0 (1.0)	6e3 (7e3)	1.0 (1.0)	4.7 (2.8)	1.2 (1.1)	2e3 (2e3)	1e5 (9e4)	48 (20)	1e7 (9e6)

is largely intrinsic to each model’s one-step predictions rather than a consequence of long rollouts. Indeed, the ratio between end-of-rollout and initial small-scale energy generally exceeds 0.7 (parenthetical values in Table 3), indicating that rollout itself contributes little additional blurring. A noteworthy outlier is DLESyM, which shows overly smooth predictions compared to ERA5. The two graph-based models (AIFS and GraphCast) tend to amplify the high-frequency content, as both their ratios compared to ERA5 and compared to their own predictions at the beginning of the rollout generally exceed 1. Due to numerical blow-up, FourCastNet exhibits large small-scale ratios.

However, we also observe that some small-scale artifacts in GraphCast U10m rollout predictions could not be detected in our energy spectra analysis (Fig. A.5), mainly due to the limited spatial extent of these perturbations that does not impact the calculation of high-frequency Fourier coefficients.

## 4 Mechanisms of Stability: Denoising and Generalization

### 4.1 Stability under noise addition

When analyzing the energy spectra of GraphCast and AIFS over time, we find that the instability originates at small spatial scales where the model creates excessive energy content, and propagates to intermediate scales (Fig. A.4). Based on this finding, we perturb the input fields of multiple models by adding a Gaussian noise  $\varepsilon \sim \mathcal{N}(0, \sigma^2)$  where  $\sigma$  is the standard deviation of each physical variable. We then compare the noisy rollout with the clean rollout to quantify how each model responds to the initial perturbation. Figure 2 shows that Aurora, Pangu, and SFNO stabilize to a constant error, while GraphCast yields an exponentially increasing error early on, and AIFS displays a mixed behavior. However, the models respond very differently to noisy inputs. Aurora and SFNO tend to denoise the inputs and produce physically realistic fields that evolve over time, while Pangu reduces the noise but converges to physically unrealistic fields, and the predictions of AIFS and GraphCast are severely perturbed by the initial noise (Fig. A.6). Although DLESyM is stable, it rapidly amplifies initial noise, which may be related to its smaller capacity (Tab. A.1). Notably, the error follows a V-shape over the first ten days: it initially decreases as the model partially denoises the input, then rises as the noisy and clean rollouts diverge toward different trajectories (Fig. 2). This V-shape marks a transition from dependence on physical initial conditions to fully generative behavior.

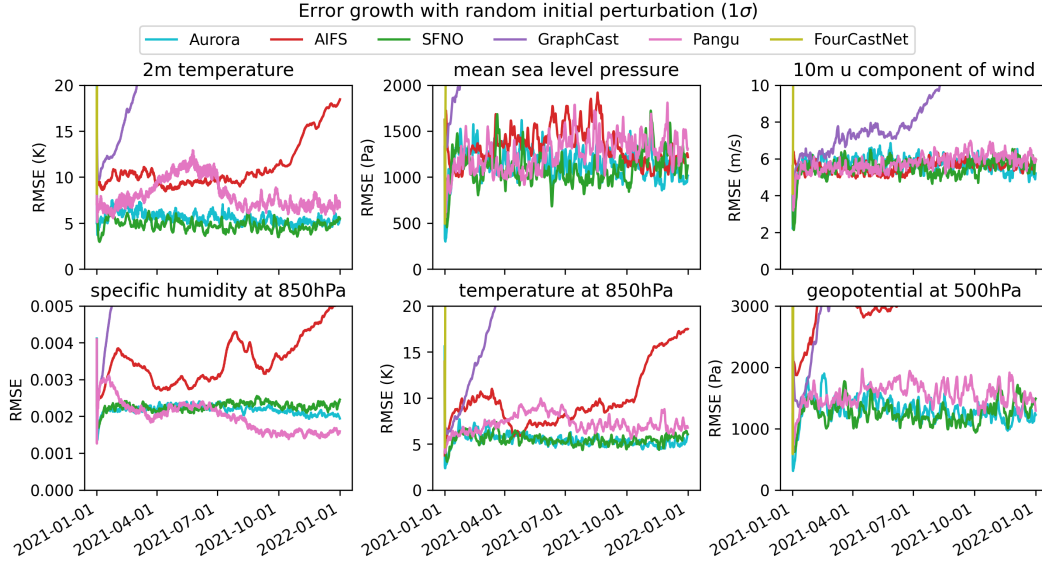


Figure 2: Error between the reference rollout and the rollout initialised with a noisy input (additive noise with  $1\sigma$  standard deviation) for five models: Aurora (cyan), AIFS (red), SFNO (green), GraphCast (purple), Pangu (pink), and six variables. The other models diverge rapidly and are shown in Fig. A.7

When the initial noise is increased from  $\sigma$  to  $10\sigma$ , the residual between noisy and clean SFNO predictions rapidly diverges, while Aurora and AIFS maintain convergence to a stable value (Fig. A.8). Pangu also converges to a stable error comparable to Aurora’s, though after a longer denoising period. These results demonstrate that both ViT models (Aurora and Pangu) progressively denoise inputs even under strong white noise and indicate Aurora’s superior stability relative to SFNO.

Because Aurora is the most robust model in our benchmark, we probe its behavior under increasingly demanding perturbations. Perturbing all dynamic variables (atmospheric and surface), Aurora successfully denoises spatially structured noise and even recovers realistic forecasts when initialized from a cat image (Fig. A.9). Perturbing only the static variables (land-sea mask, soil type, and orography) causes rollouts to degenerate (Fig. A.10), though Section 5 shows this reflects Aurora’s sensitivity to corrupted inputs rather than an architectural necessity for static variables.

## 4.2 Absence of memorization

The ability to generate realistic weather from noise warrants a deeper investigation into whether the models have learned generalizable atmospheric dynamics or are merely overfitting to specific sequences in the training set. This section focuses on Aurora and SFNO experiments as the previous section showed that they denoise inputs to realistic fields. First, we run five rollouts initialized from different pure white Gaussian noise and compute the pixel-wise standard deviation across the rollouts to assess trajectory diversity. We obtain values comparable to the training set’s standard deviation for surface variables, while atmospheric variables are approximately three times smaller (Fig. A.13). This sustained variability demonstrates that each randomly initialized rollout generates a unique trajectory, rather than collapsing to a single memorized sequence.

The second test examines whether stable models simply replay memorized training samples. Following previous work on memorization in diffusion models [6, 13, 33], a sample  $X_t$  is said to be memorized if it is significantly closer to its first neighbor in the training dataset than to its second neighbor (Appendix C.3). Figure A.14 shows that the distance ratio remains close to 1 throughout the one-year rollout for both Aurora and SFNO, indicating no systematic preference for the nearest training neighbor and thus no evidence of memorization. In summary, Aurora and SFNO converge toward the seasonal cycle as a dynamic attractor, but this behavior reflects genuine generalization rather than memorization of training trajectories.

## 4.3 Influence of the time embedding

Most AI weather models are given time information as input, both the absolute time of the input and the lead time of the prediction. To test whether the time embedding anchors the model’s output to the correct season, we conduct a seasonal

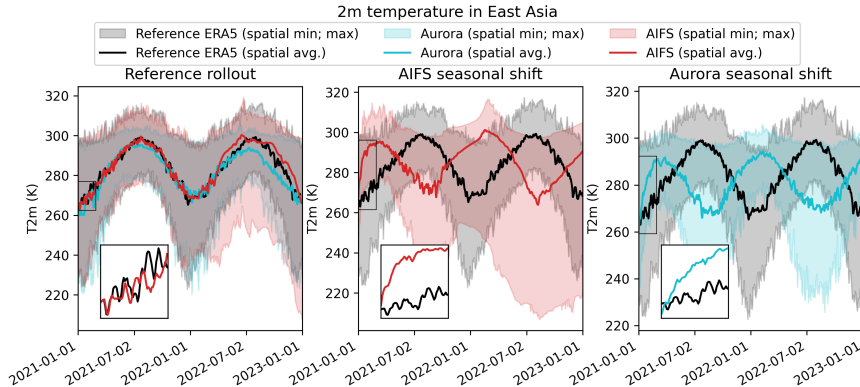


Figure 3: 2-meter temperature in East Asia for Aurora and AIFS initialized on January 1st, 2021 (left column), AIFS (middle column), and Aurora (right column) initialized with physical values from January 1st, 2021 and time information of June 1st, 2021. The solid lines show the regional average, the shaded areas extend from the minimal to the maximal temperature over the region. The subplots show the first two months. Time series are depicted at a daily resolution (at T00) for easier visualization.

shift experiment. We initialize a 2-year Aurora and AIFS rollout with physical inputs from January 1, 2021, but provide the model with time information corresponding to June 1, 2021. Figure 3 shows that the predictions diverge from the reference within a few days, converging instead to a trajectory consistent with the June seasonal cycle. This indicates that Aurora and AIFS rapidly adjust the physical state to match the provided time embedding, overriding the January initial conditions within days. In addition, fixing the date constant throughout the rollout similarly drives the model toward a time-invariant state with no seasonal cycle, confirming that the time embedding drives long-term temporal structure (not shown).

## 5 Design choices for achieving realistic rollouts

Having established that Aurora exhibits superior long-rollout stability among the nine models studied, we now investigate which design choices drive this behavior through systematic ablation experiments. We train a small Aurora variant (denoted Aurora<sub>s</sub>, 113M parameters) from random initialization across multiple configurations, varying one component at a time, and we find that stability is remarkably insensitive to most design choices we tested. Aurora<sub>s</sub> is trained on ERA5 data from 1979 to 2019, with 2020 serving as validation, and 2021-2024 as test set. Training is conducted on 8 GPUs for 60k steps, with a per-GPU batch size 1, and no model parallelization. Unless otherwise mentioned, it is trained with 6-hour lead time and 0.25° resolution.

### 5.1 Architectural invariants: what does not determine stability

We first vary the components of the Swin3D attention mechanism. Changing the window size from the default (2, 6, 12) to (2, 3, 6) or (2, 12, 24), removing window shifting, or varying the patch size across 1, 2, and 4 all produce stable rollouts with accurate seasonality.

We next test normalization, motivated by the expectation that Layer Normalization prevents value divergence and thus promotes stability. Replacing Layer Normalization with RMSNorm does not affect stability (Fig. 4b, second row). Reducing the number of atmospheric levels from 13 to 3 likewise preserves stable and seasonal rollouts, despite substantially reducing the amount of training data and the vertical resolution of the atmospheric representation (Fig. 4b, first row).

Static variables (land-sea mask, soil type, and orography) might be expected to play a stabilizing role, since Section 4.1 shows that corrupting them at inference time causes full degeneration. However, training Aurora<sub>s</sub> entirely without static variables also produces a stable model that preserves seasonality and retains denoising ability. This apparent contradiction is resolved by noting that the two experiments ask different questions: a model trained without static variables learns not to rely on them, while a model trained with them becomes sensitive to their corruption at inference time.

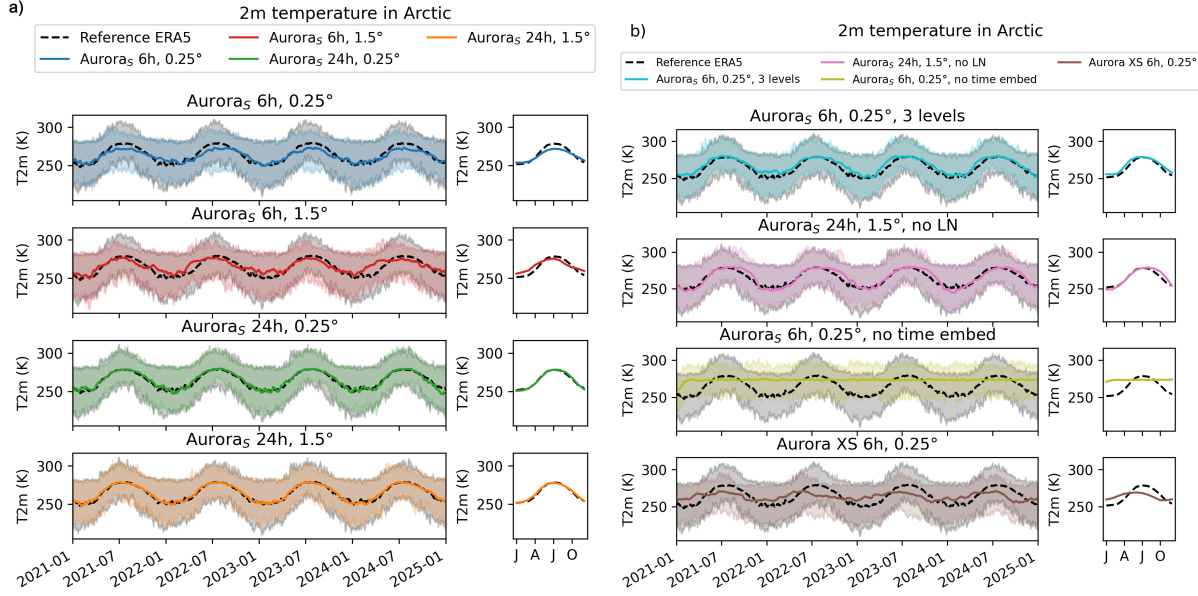


Figure 4: 4-year rollout of 2-meter temperature for a) four small Aurora models trained from scratch with different spatial resolutions ( $0.25^\circ$  and  $1.5^\circ$ ) and lead times (6 hours and 24 hours), b) small Aurora with three atmospheric levels (500 hPa, 850 hPa, 1000 hPa) instead of 13, with RMS normalization instead of Layer Normalization, without time embedding, extra-small model (21M parameters). The right panels show the monthly seasonal cycle.

Finally, removing the absolute time embedding suppresses all explicit information about long-term dynamics. The rollout does not blow up but the model converges to a physically stable state without seasonality (Fig. 4b, third row). Time embedding is therefore not a condition for dynamical stability, but is necessary for climatological accuracy.

Taken together, these results suggest that stability arises from a combination of factors rather than from any particular inductive bias of the architecture. Notably, reducing the parameter count from 113M to 21M — by shrinking the encoder depth from (2, 6, 2) to (2, 2, 2) and the embedding dimension from 256 to 128 — eliminated the realistic seasonal cycle (Fig. 4b, fourth row), suggesting a minimum model capacity threshold for seasonality.

## 5.2 Temporal and spatial scales during training

To examine the influence of spatiotemporal resolution during training, we train Aurora<sub>S</sub> from random initialization on four configurations that combine spatial resolutions  $0.25^\circ$  and  $1.5^\circ$ , and lead times 6 hours and 24 hours. Figure 4a shows that the four Aurora<sub>S</sub> models produce stable 4-year rollouts with seasonality. The seasonality metric defined in Section 3 indicates that both 24-hour models preserve accurate seasonality across the full four-year rollout. For the 6-hour models, the metric is conservative and flags a loss of seasonality after 381 days ( $0.25^\circ$ ) and 244 days ( $1.5^\circ$ ), consistent with the visible drift in Fig. 4a and Table A.4. The Fourier spectra (Fig. A.15) confirm that  $1.5^\circ$  models produce smoother predictions than  $0.25^\circ$  models, though the degree of smoothing does not significantly worsen during rollout. By contrast,  $0.25^\circ$  models accumulate small-scale spectral energy beyond the ERA5 reference during rollout, though neither blows up. This effect is stronger in the 24-hour model than the 6-hour model.

## 5.3 Stability and seasonality training dynamics

Since all Aurora<sub>S</sub> rollouts preserve seasonal fluctuations, we move beyond detecting their loss to quantifying seasonal accuracy. We assess the ability of the model to reproduce long-term behavior by computing the monthly seasonal cycle over the four-year rollout and comparing it with the ERA5 monthly cycle over the same time period (2021-2024). The RMSE between the monthly seasonal cycles then serves as a quantitative measure of how accurate a model is in reproducing the true seasonal cycle. Figure 5 shows that the seasonal cycle error generally decreases as the training progresses, although there can be significant differences between consecutive training steps. All Aurora<sub>S</sub> models match the seasonal accuracy of the full Aurora model (1.3B parameters, [3]) within 60k training steps, despite the large difference in model capacity. This suggests that long training of the large model does not impact the seasonality of long rollouts, although it is essential to improve short and medium-term accuracy.

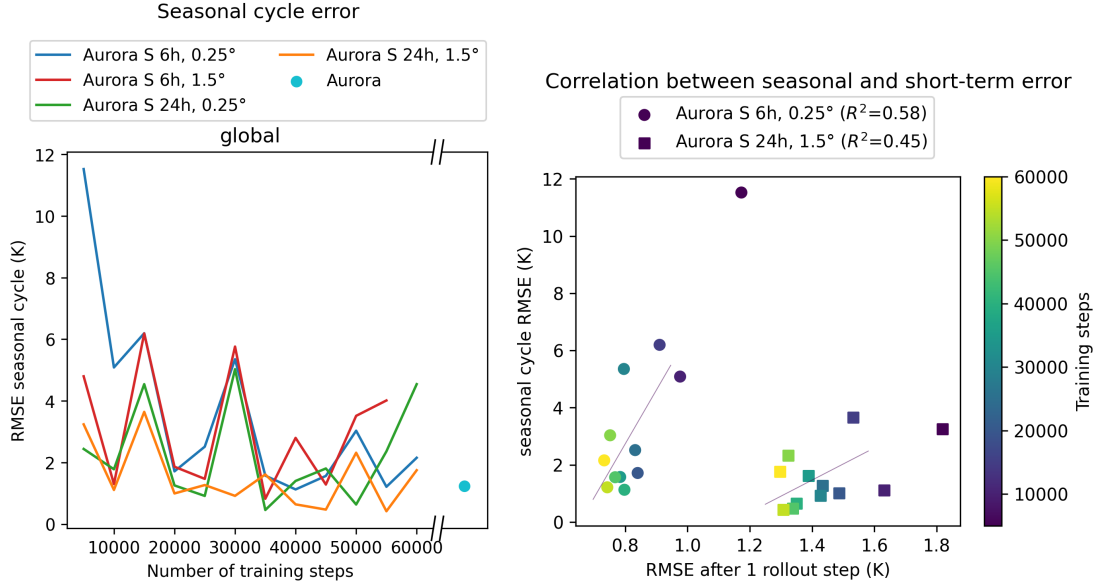


Figure 5: (left) RMSE between the monthly seasonal cycle of the  $Aurora_S$  models and ERA5, as a function of the number of training steps. The seasonal cycle from the large Aurora model [3] is shown with the cyan dot. (right) On the horizontal axis, 2-meter temperature RMSE after one rollout step (6-hour or 24-hour lead time depending on the model). On the vertical axis, 2-meter temperature seasonal cycle RMSE. Each model is evaluated at different training steps indicated by the colored markers. The linear regression for each model is shown with the thin line and the coefficient of determination is indicated in the legend.

The coarsest configuration (24-hour,  $1.5^\circ$ ) has the lowest seasonal cycle error and its accuracy is less dependent on the training step. This configuration mirrors the design of most climate emulators, which trade fine-scale detail for long-term stability. While Fig. 5a clearly indicates that seasonal accuracy improves during training, there is only moderate correlation between short-term error and seasonal accuracy of the models at different stages in their training (Fig. 5b). Short-term error constantly decreases during training, while long-term seasonality is only a byproduct.

## 6 Extreme Events Statistics on Stable Rollouts

The preceding sections show that several models produce stable rollouts preserving seasonality over year-long time scales. Here we examine whether stable long rollouts preserve the distributional properties needed for climate applications. To this end, we focus on the extreme temperature events derived from 10-year rollouts of Aurora, SFNO, and DLESyM, and compare their statistics with ERA5. All models are initialized on January 1st, 2021 and rolled out for 10 years (14,700 steps). The first four years are used as a statistical comparison against ERA5 for the same time period. We define hot (cold) events as timesteps where the regional maximum (minimum) exceeds the 90th (falls below the 10th) percentile of the ERA5 climatology; full details are in Appendix E.

The statistical occurrence of extreme events is evaluated with quantile-quantile plots for hot and cold events (Fig. 6). For hot events, points below the diagonal indicate that Aurora and DLESyM underestimate the temperature of hot events. For SFNO, results are region-dependent as hot events are underestimated in the Southern regions but overestimated in the three Northern regions under study. For cold events, Aurora and DLESyM have lighter tails, while SFNO exhibits a slight cold bias in the Southern regions (Fig. A.17), leading it to produce colder extremes in Australia and the Amazon. A frequency analysis shows that no model consistently reproduces extreme event frequency of ERA5 and no model is clearly better than the others (Fig. A.16). Overall, our results show that Aurora, SFNO, and DLESyM generate physically plausible extreme events during long rollouts, though their magnitude and frequency do not perfectly match ERA5.

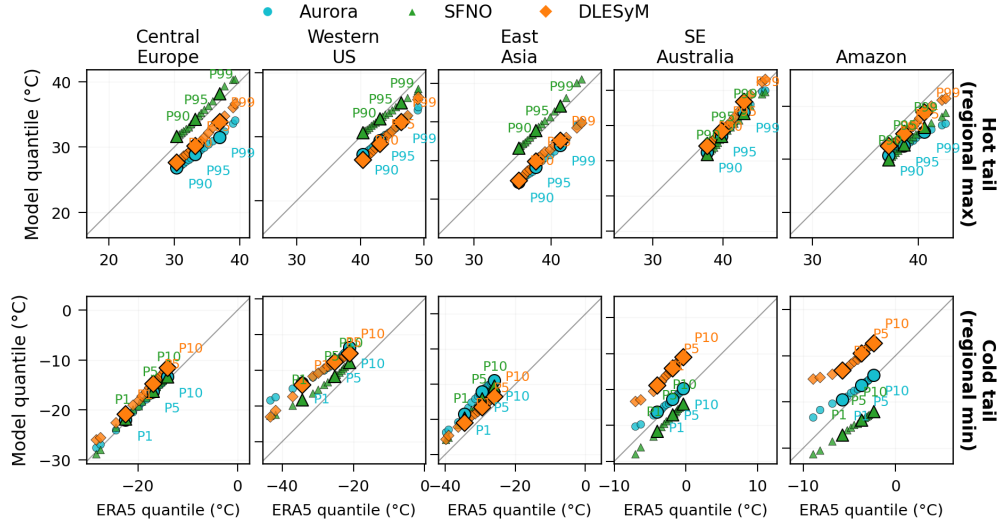


Figure 6: QQ plots comparing ERA5 and the model tail quantiles of regional spatial maximum (hot, top) and minimum (cold, bottom) across five regions. Only points below the 10th and above the 90th percentile are shown.

## 7 Limitations and Conclusion

Most work on data-driven weather models targets short- to medium-range accuracy improvements. In this study, we first thoroughly quantify, compare, and benchmark longer rollout performance of nine leading AI weather models, including deterministic and probabilistic models. While our metrics provide the first quantitative description of rollout instability and are robust to the choice of initial date, some local unrealistic patterns could not be detected until they degenerate to larger scales. Nevertheless, our metrics could guide the development of AI weather models that aim at long-term predictions.

By perturbing the initial conditions with different types of noise, we show that the large stable models (SFNO, Aurora, and Pangu to a lesser extent) denoise inputs with progressive low-pass filtering to realistic predictions. For Aurora and SFNO, this extends to generalization capabilities from pure noise, towards a seasonal attractor that yields diverse realistic trajectories.

We then investigate Aurora — the most stable model in our benchmark — through systematic ablation studies on architecture and training data choices. Aurora is robust to individual architectural changes, suggesting that the core architecture offers denoising abilities that maintain stable long rollouts. The efficiency of Aurora’s training is consistent with Willard et al. [30], which demonstrates rapid convergence of 2D Swin v2 models; both that work and the present study nonetheless capture only a partial view of model capabilities. Our ablation studies are restricted to ViT and future work should extend these analyses to other architectures.

The three models yielding stable and physically realistic long rollouts (SFNO, Aurora, DLESyM) produce realistic extreme events over 10-year rollouts, although they tend to be less extreme and frequent than the reference period from ERA5, as commonly reported [32]. This shows the potential of AI weather models for studying extreme events, though this potential is not yet fully realized given the remaining biases in magnitude and frequency.

It is important to note that this work does not address the influence of climate change on long rollouts. Models have been trained on historical data, hence they are not expected to be robust or to give physically realistic results under distribution shifts. Nevertheless, identifying models with stable long-rollout behavior is a necessary first step toward future climate-aware AI systems.

## Acknowledgements

This work was supported under project IDs a01 and a122 as part of the Swiss AI Initiative, through a grant from the ETH Domain and computational resources provided by the Swiss National Supercomputing Centre (CSCS) under the Alps infrastructure. This research was primarily supported by the ETH AI Center through an ETH AI Center postdoctoral fellowship to Fanny Lehmann. The authors thank sincerely Andrin Zoller for running ensemble rollout forecasts of AIFS-ens.

## **Data and Code Availability**

The publicly available ERA5 dataset was downloaded from WeatherBench2 [28]. For Aurora, AIFS, and DLESyM, we use the reference code repository to run the inference of the models, respectively <https://github.com/microsoft/aurora>, <https://github.com/ecmwf/anemol-inference>, <https://github.com/AtmosSci-DLES/DLESyM>. The other models are used through Nvidia Earth2Studio platform <https://github.com/NVIDIA/earth2studio>. The code to compute the stability metrics is available at <https://github.com/lehmannfa/ai-weather-stability>.

## References

- [1] V. Armeigoiu. Memory-Conditioned Flow-Matching for Stable Autoregressive PDE Rollouts, Feb. 2026.
- [2] K. Bi, L. Xie, H. Zhang, X. Chen, X. Gu, and Q. Tian. Accurate medium-range global weather forecasting with 3D neural networks. *Nature*, 619(7970):533–538, July 2023. Pangu.
- [3] C. Bodnar, W. P. Bruinsma, A. Lucic, M. Stanley, A. Allen, J. Brandstetter, P. Garvan, M. Riechert, J. A. Weyn, H. Dong, J. K. Gupta, K. Thambiratnam, A. T. Archibald, C.-C. Wu, E. Heider, M. Welling, R. E. Turner, and P. Perdikaris. A foundation model for the Earth system. *Nature*, May 2025.
- [4] M. Bonavita. On Some Limitations of Current Machine Learning Weather Prediction Models. *Geophysical Research Letters*, 51(12):e2023GL107377, June 2024.
- [5] B. Bonev, T. Kurth, C. Hundt, J. Pathak, M. Baust, K. Kashinath, and A. Anandkumar. Spherical Fourier neural operators: Learning stable dynamics on the sphere. In A. Krause, E. Brunskill, K. Cho, B. Engelhardt, S. Sabato, and J. Scarlett, editors, *Proceedings of the 40th international conference on machine learning*, volume 202 of *Proceedings of machine learning research*, pages 2806–2823. PMLR, July 2023.
- [6] T. Bonnaire, R. Urfin, G. Biroli, and M. Mézard. Why Diffusion Models Don’t Memorize: The Role of Implicit Dynamical Regularization in Training, Oct. 2025. arXiv:2505.17638 [cs].
- [7] J. Brandstetter, D. Worrall, and M. Welling. Message Passing Neural PDE Solvers. 2022.
- [8] A. Chattopadhyay, Y. Q. Sun, and P. Hassanzadeh. Challenges of learning multi-scale dynamics with AI weather models: Implications for stability and one solution, Dec. 2024. long rollouts.
- [9] L. Chen, X. Zhong, F. Zhang, Y. Cheng, Y. Xu, Y. Qi, and H. Li. FuXi: a cascade machine learning forecasting system for 15-day global weather forecast. *npj Climate and Atmospheric Science*, 6(1):190, Nov. 2023.
- [10] G. Couairon, C. Lessig, A. Charantonis, and C. Monteleoni. ArchesWeather: An efficient AI weather forecasting model at 1.5{deg} resolution, May 2024.
- [11] N. Cresswell-Clay, B. Liu, D. R. Durran, Z. Liu, Z. I. Espinosa, R. A. Moreno, and M. Karlbauer. A Deep Learning Earth System Model for Efficient Simulation of the Observed Climate. *AGU Advances*, 6(4):e2025AV001706, Aug. 2025.
- [12] F. Gallusser, S. Hentschel, A. Krause, and A. Hotho. Exploring Design Choices for Autoregressive Deep Learning Climate Models, May 2025. long rollouts.
- [13] X. Gu, C. Du, T. Pang, C. Li, M. Lin, and Y. Wang. On Memorization in Diffusion Models, 2023. Version Number: 2.
- [14] H. Guan, T. Arcomano, A. Chattopadhyay, and R. Maulik. LUCIE: A Lightweight Uncoupled Climate Emulator with long-term stability and physical consistency for O(1000)-member ensembles, 2024.
- [15] H. Hersbach, B. Bell, P. Berrisford, S. Hirahara, A. Horányi, J. Muñoz-Sabater, J. Nicolas, C. Peubey, R. Radu, D. Schepers, A. Simmons, C. Soci, S. Abdalla, X. Abellan, G. Balsamo, P. Bechtold, G. Biavati, J. Bidlot, M. Bonavita, G. De Chiara, P. Dahlgren, D. Dee, M. Diamantakis, R. Dragani, J. Flemming, R. Forbes, M. Fuentes, A. Geer, L. Haimberger, S. Healy, R. J. Hogan, E. Hólm, M. Janisková, S. Keeley, P. Laloyaux, P. Lopez, C. Lupu, G. Radnoti, P. de Rosnay, I. Rozum, F. Vamborg, S. Villaume, and J.-N. Thépaut. The ERA5 global reanalysis. *Quarterly Journal of the Royal Meteorological Society*, 146(730):1999–2049, July 2020.
- [16] M. Karlbauer, N. Cresswell-Clay, D. R. Durran, R. A. Moreno, T. Kurth, B. Bonev, N. Brenowitz, and M. V. Butz. Advancing Parsimonious Deep Learning Weather Prediction Using the HEALPix Mesh. *Journal of Advances in Modeling Earth Systems*, 16(8):e2023MS004021, Aug. 2024.
- [17] D. Kochkov, J. Yuval, I. Langmore, P. Norgaard, J. Smith, G. Mooers, M. Klöwer, J. Lottes, S. Rasp, P. Düben, S. Hatfield, P. Battaglia, A. Sanchez-Gonzalez, M. Willson, M. P. Brenner, and S. Hoyer. Neural general circulation models for weather and climate. *Nature*, 632(8027):1060–1066, Aug. 2024.
- [18] R. Lam, A. Sanchez-Gonzalez, M. Willson, P. Wirsberger, M. Fortunato, F. Alet, S. Ravuri, T. Ewalds, Z. Eaton-Rosen, W. Hu, A. Merose, S. Hoyer, G. Holland, O. Vinyals, J. Stott, A. Pritzel, S. Mohamed, and P. Battaglia. Learning skillful medium-range global weather forecasting. *Science*, page eadi2336, Nov. 2023.
- [19] S. Lang, M. Alexe, M. Chantry, J. Dramsch, F. Pinault, B. Raoult, M. C. A. Clare, C. Lessig, M. Maier-Gerber, L. Magnusson, Z. B. Bouallègue, A. P. Nemesio, P. D. Dueben, A. Brown, F. Pappenberger, and F. Rabier. AIFS - ECMWF’s data-driven forecasting system, June 2024.
- [20] S. Lang, M. Alexe, M. C. A. Clare, C. Roberts, R. Adewoyin, Z. B. Bouallègue, M. Chantry, J. Dramsch, P. D. Dueben, S. Hahner, P. Maciel, A. Prieto-Nemesio, C. O’Brien, F. Pinault, J. Polster, B. Raoult, S. Tietsche, and

- M. Leutbecher. AIFS-CRPS: Ensemble forecasting using a model trained with a loss function based on the Continuous Ranked Probability Score, Dec. 2024. S2S.
- [21] P. Lippe, B. Veeling, P. Perdikaris, R. Turner, and J. Brandstetter. PDE-refiner: Achieving accurate long rollouts with neural PDE solvers. In A. Oh, T. Naumann, A. Globerson, K. Saenko, M. Hardt, and S. Levine, editors, *Advances in neural information processing systems*, volume 36, pages 67398–67433. Curran Associates, Inc., 2023.
- [22] O. Loegel, J. Talib, F. Vitart, J. Hoffmann, and M. Chantry. The AI Weather Quest: an international competition for sub-seasonal forecasting with AI. *Machine Learning: Earth*, 1(1):010701, Dec. 2025.
- [23] M. McCabe, P. Harrington, S. Subramanian, and J. Brown. Towards stability of autoregressive neural operators. *Transactions on Machine Learning Research*, 2023.
- [24] F. Nie and Y. Suzuki. JAWS: Enhancing Long-term Rollout of Neural PDE Solvers via Spatially-Adaptive Jacobian Regularization, 2026.
- [25] J. Pathak, S. Subramanian, P. Harrington, S. Raja, A. Chattopadhyay, M. Mardani, T. Kurth, D. Hall, Z. Li, K. Azzadenesheli, P. Hassanzadeh, K. Kashinath, and A. Anandkumar. FourCastNet: A Global Data-driven High-resolution Weather Model using Adaptive Fourier Neural Operators, Feb. 2022.
- [26] C. Pedersen, L. Zanna, and J. Bruna. Thermalizer: Stable autoregressive neural emulation of spatiotemporal chaos, Mar. 2025. long rollout.
- [27] I. Price, A. Sanchez-Gonzalez, F. Alet, T. R. Andersson, A. El-Kadi, D. Masters, T. Ewalds, J. Stott, S. Mohamed, P. Battaglia, R. Lam, and M. Willson. Probabilistic weather forecasting with machine learning. *Nature*, Dec. 2024. GenCast.
- [28] S. Rasp, S. Hoyer, A. Merose, I. Langmore, P. Battaglia, T. Russel, A. Sanchez-Gonzalez, V. Yang, R. Carver, S. Agrawal, M. Chantry, Z. B. Bouallegue, P. Dueben, C. Bromberg, J. Sisk, L. Barrington, A. Bell, and F. Sha. WeatherBench 2: A benchmark for the next generation of data-driven global weather models, Jan. 2024.
- [29] O. Watt-Meyer, B. Henn, J. McGibbon, S. K. Clark, A. Kwa, W. A. Perkins, E. Wu, L. Harris, and C. S. Bretherton. ACE2: Accurately learning subseasonal to decadal atmospheric variability and forced responses, Nov. 2024.
- [30] J. D. Willard, P. Harrington, S. Subramanian, A. Mahesh, T. A. O’Brien, and W. D. Collins. Analyzing and Exploring Training Recipes for Large-Scale Transformer-Based Weather Prediction. *Artificial Intelligence for the Earth Systems*, 4(2):240061, Apr. 2025.
- [31] H. Wu, Y. Gao, R. Shu, K. Wang, R. Gou, C. Wu, X. Liu, J. He, S. Cao, J. Fang, X. Shi, F. Tao, Q. Song, S. Ji, Y. Xiang, Y. Sun, J. Li, F. Xu, H. Dong, H. Wang, F. Zhang, P. Zhao, X. Wu, Q. Wen, D. Chen, and X. Huang. Advanced long-term earth system forecasting by learning the small-scale nature, 2025.
- [32] W. Xu, K. Chen, T. Han, H. Chen, W. Ouyang, and L. Bai. ExtremeCast: Boosting Extreme Value Prediction for Global Weather Forecast. 2024. extreme values.
- [33] T. Yoon, J. Y. Choi, S. Kwon, and E. K. Ryu. Diffusion probabilistic models generalize when they fail to memorize. In *ICML 2023 workshop on structured probabilistic inference & generative modeling*, 2023.
- [34] H. Zhou and S. Cheng. Improving long-term autoregressive spatiotemporal predictions: A proof of concept with fluid dynamics. *Computer Methods in Applied Mechanics and Engineering*, 447:118332, Dec. 2025.

## A Weather and Climate Models

Table A.1: Non exhaustive summary of state-of-the-art AI weather and climate models referenced in this work. Spatial resolutions in degrees can be approximated as:  $0.25^\circ \simeq 25\text{km}$ ,  $1.0^\circ \simeq 110\text{km}$ . Training data come from ERA5 if not specified otherwise.

Model reference	Architecture	# param.	Spatial res.	Training period & Lead time
AIFS [19]	Graph Transformer	253M	N320 grid $\simeq 31\text{km}$	1979-2022 6h
Aurora [3]	3D Swin Transformer	1.3B	$0.25^\circ$	1979-2020 6h
FourCastNet [25]	Adaptive FNO	75M	$0.25^\circ$	1979-2015 6h
FuXi [9]	3D Swin Transformer	4.7B	$0.25^\circ$	1979-2015 6h
GenCast [27]	Diffusion model	57M	$0.25^\circ$	1979-2017 12h
GraphCast [18]	Graph Neural Network	36.7M	$0.25^\circ$	1979-2017 6h
PanguWeather [2]	3D Swin Transformer and Earth-specific Transformer	256M	$0.25^\circ$	1979-2017 1h-24h
SFNO [5]	SFNO	289M	$0.25^\circ$	1979-2015 6h
ACE2 [29]	SFNO	450M	$1.0^\circ$	1940-1995, 2011-2019, 2021-2022 6h
ArchesWeather [10]	3D Swin Transformer	84M	$1.5^\circ$	1979-2018 24h
DLESyM [11]	ConvNeXt and GRU	3.5M (at-mos.)	(at- HEALPix 64 ( $\simeq 1^\circ$ ))	1983-2016 6h (atmos.)
DLWP-HPX [16]	ConNeXt and GRU	9.8M	HEALPix 64 ( $\simeq 1^\circ$ )	1979-2012 3h
LUCIE [14]	SFNO		T30 grid ( $\simeq 3.75^\circ$ )	10 years

## B Definitions of stability metrics

### B.1 Blow-up

The blow-up of a rollout is defined from the two timeseries of minimum and maximum values over the globe  $\Omega$

$$\hat{u}_{min}(t) = \min_{x,y \in \Omega} \hat{u}(x,y,t) \quad ; \quad \hat{u}_{max}(t) = \max_{x,y \in \Omega} \hat{u}(x,y,t) \quad (1)$$

where  $\hat{u}$  is the prediction of the physical variable  $u$ . As the same procedure is applied to  $\hat{u}_{min}$  and  $\hat{u}_{max}$ , the following describes the computation for  $\hat{u}_{min}$  only. First, an average rolling window of 4 days is applied to smooth small-scale fluctuations. Then, a linear regression is applied on the log-transform of  $\hat{u}_{min}$  over time windows of 30 days. If the coefficient of determination is larger than 0.9 for a given time window,  $\hat{u}_{min}$  exhibits an exponential growth over this time window. The beginning of the first time window satisfying these criteria is then defined as the time when the model blows up. The reported global blow-up time in Table 1 is the earliest blow-up time between  $\hat{u}_{min}$  and  $\hat{u}_{max}$ .

For FourCastNet, the window size for applying the linear regression was reduced to 10 days because the blow-up happens too quickly and the model saturates at some constant value after the blow-up.

### B.2 Loss of seasonality

Due to the large spatial extent of seasonal fluctuations, seasonality is quantified from the large-scale energy spectra. For each variable and each timestep of the rollout, the energy spectrum is averaged over wavelengths larger than

5000 km, which correspond to planetary patterns (the energy spectrum  $\mathcal{E}$  at wavelength  $\lambda$  is the amplitude of the Fourier coefficient at  $\lambda$ , taken along the longitude direction and averaged latitude-wise with latitude-dependent weights)

$$\hat{\mathcal{E}}_{large}(t) = \frac{1}{n_{large}} \sum_{\lambda \geq 5000\text{km}} \hat{\mathcal{E}}(\lambda, t) \quad (2)$$

Large-scale energy spectra are also computed from the reference ERA5 between 1990 and 2019 to quantify the climatological fluctuations. The climatological range  $\mathcal{E}_{large}^{range}$  is defined as the difference between the maximum and minimum observed energy spectrum on a given day  $d$

$$\mathcal{E}_{large}^{range}(d) = \max_{y \in [1990, 2019]} \mathcal{E}_{large}(d, y) - \min_{y \in [1990, 2019]} \mathcal{E}_{large}(d, y) \quad (3)$$

The rollout is said to lose seasonality if its large-scale energy spectrum  $\hat{\mathcal{E}}_{large}$  deviates from the observed ERA5  $\mathcal{E}_{large}$  by more than  $\mathcal{E}_{large}^{range}$  for at least 45 days. Figure A.1 illustrates the loss of seasonality for Pangu on 2-meter temperature after 182 days while SFNO preserves seasonality for the entire duration studied here.

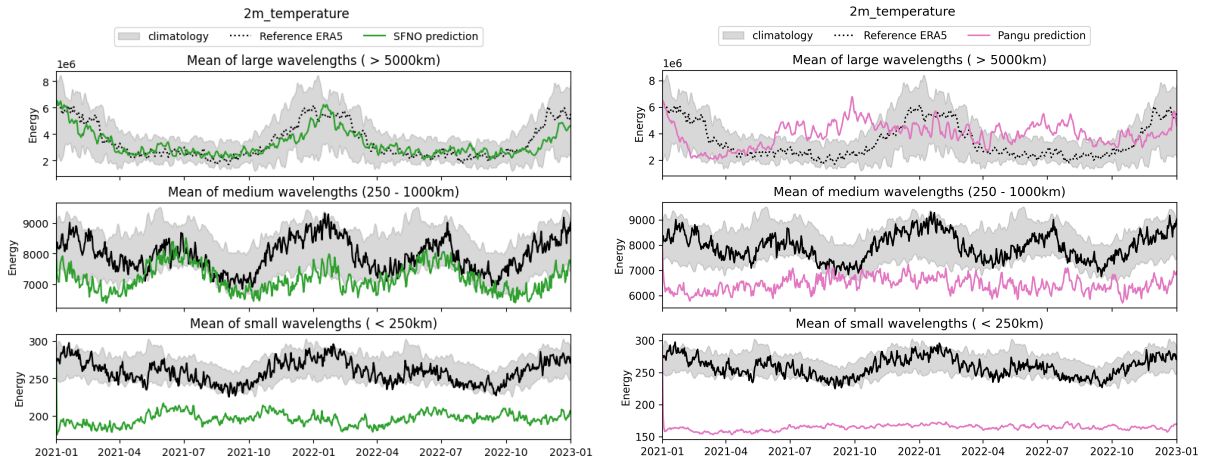


Figure A.1: Energy spectra of 2-meter temperature rollouts for SFNO (left) and Pangu (right). The spectra are averaged into three bands: large wavelengths (larger than 5000 km), medium wavelengths (between 250 and 1000 km), and small wavelengths (smaller than 250 km). Energy spectra from ERA5 is shown in black. For a given day of the year, the grey area extends from the minimum to the maximum observed energy spectrum on this day between 1990 and 2019.

### B.3 Small-scale artifacts

Small-scale artifacts are quantified from the energy spectrum averaged over wavelengths smaller than 250 km,  $\mathcal{E}_{small}$ . Two ratios of time-averaged energy spectra are computed. First, the ratio between the prediction and reference, averaged over the last 30 days of the rollout. If blow-up was detected, the last 30 days before the blow-up time are considered. Second, the ratio between average predictions in the last 30 days and the average predictions in the first two days. The former quantifies the small-scale energy content relative to ERA5 while the latter assesses the influence of the rollout on small spatial features.

### B.4 Sensitivity to initial conditions

This section reports the average and standard deviation of the blow-up, loss of seasonality, and small-scale artifacts metrics, computed over five rollouts with different initial conditions (January 1st, 2021 at time T00, T06, T12, T18, December 1st, 2021). For probabilistic models, five rollouts with different seeds on January 1st, 2021 are reported. Two ensemble members are aggregated (meaning that the average and standard deviations are computed on ten time series).

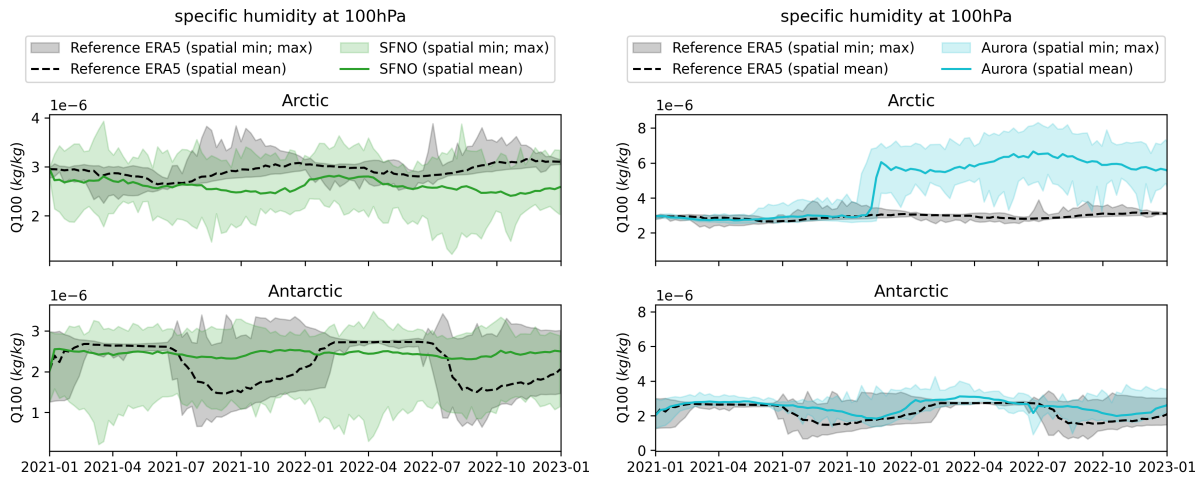


Figure A.2: 100 hPa specific humidity rollouts with SFNO (left) and Aurora (right). Rollouts are initialized on January 1st, 2021. The solid lines show the spatial averaged across Arctic and Antarctic for the reference ERA5 (black) and the model (color). The shaded areas extend from the minimum to the maximum temperature over the Arctic and Antarctic for ERA5 (grey) and the model (color).

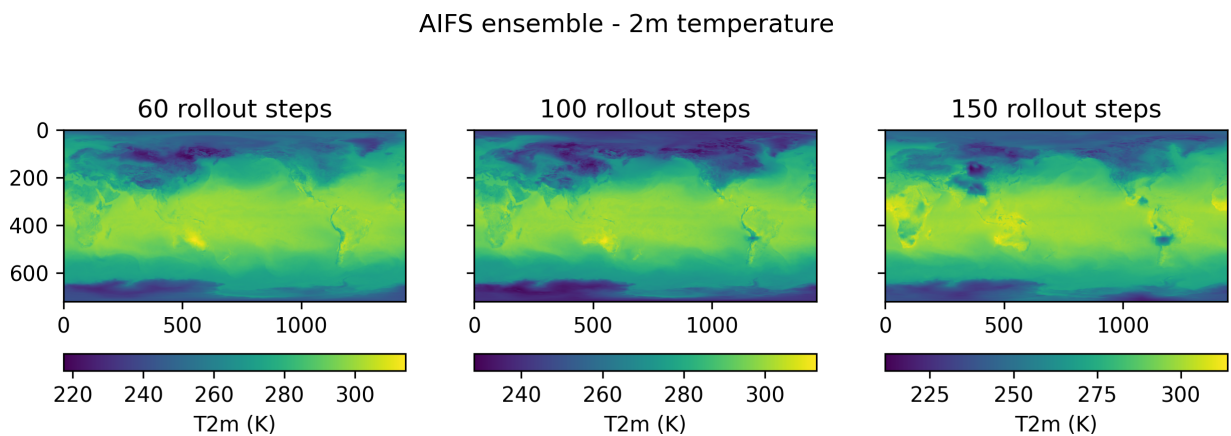


Figure A.3: Predictions of 2-meter temperature after 60, 100, and 150 rollout steps with AIFS ensemble [20]

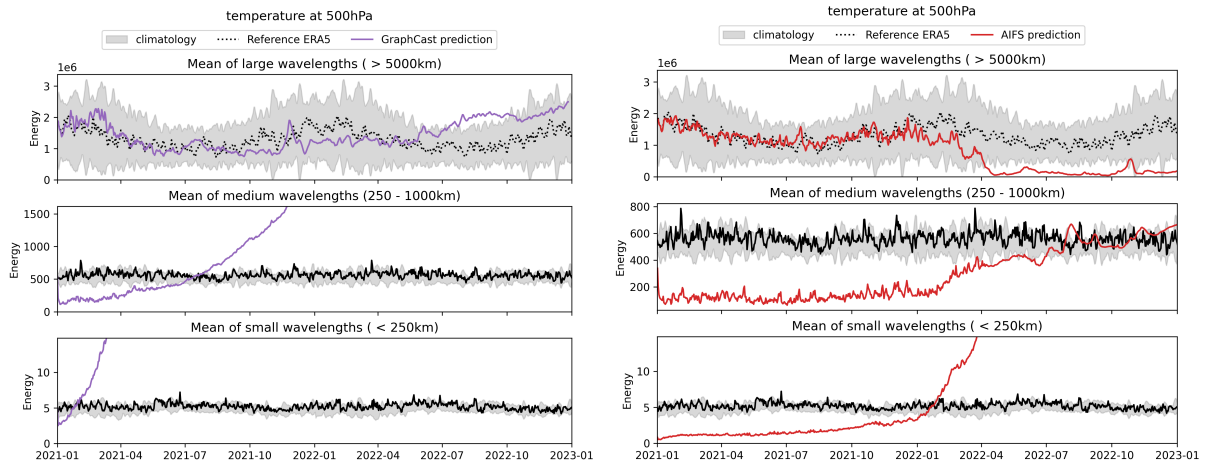


Figure A.4: Energy spectra of 500 hPa temperature rollouts for GraphCast (left) and AIFS (right). The spectra are averaged into three bands: large wavelengths (larger than 5000 km), medium wavelengths (between 250 and 1000 km), and small wavelengths (smaller than 250 km). Energy spectra from ERA5 is shown in black. For a given day of the year, the grey area extends from the minimum to the maximum observed energy spectrum on this day between 1990 and 2019.

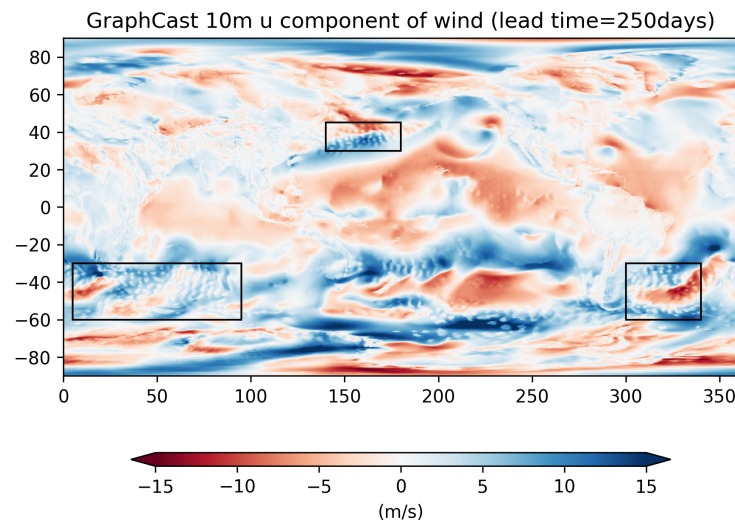


Figure A.5: 10-meter eastward component of wind predicted by GraphCast after 250 rollout days. Boxes highlight regions where small-scale artifacts are especially visible.

Table A.2: Number of days until the model predictions blow-up. Same as Table 1 but with mean and standard deviation across five rollouts initialized on different dates

Model	T2m	U10m	MSLP	Z500	T500	Q500	U300	T100	Q100
Aurora	730 ± 0.0	730 ± 0.0	730 ± 0.0	730 ± 0.0	730 ± 0.0	730 ± 0.0	730 ± 0.0	730 ± 0.0	365 ± 333.7
SFNO	730 ± 0.0	730 ± 0.0	730 ± 0.0	730 ± 0.0	730 ± 0.0	730 ± 0.0	730 ± 0.0	730 ± 0.0	730 ± 0.0
AIFS	82 ± 93.9	730 ± 0.0	730 ± 0.0	18 ± 2.5	730 ± 0.0	730 ± 0.0	726 ± 8.9	730 ± 0.0	667 ± 140.4
GraphCast	393 ± 105.2	399 ± 17.4	319 ± 89.2	277 ± 38.2	339 ± 58.4	402 ± 88.1	465 ± 242.4	468 ± 70.9	305 ± 89.0
GenCast	84 ± 8.2	730 ± 0.0	82 ± 5.6	76 ± 6.1	78 ± 6.2	730 ± 0.0	730 ± 0.0	98 ± 8.0	443 ± 335.5

Table A.3: Number of days until the model predictions lose seasonality. Same as Table 2 but with mean and standard deviation across five rollouts initialized on different dates

Model	T2m	U10m	MSLP	Z500	T500	Q500	U300	T100	Q100
Aurora	730 ± 0.0	730 ± 0.0	730 ± 0.0	730 ± 0.0	730 ± 0.0	730 ± 0.0	730 ± 0.0	730 ± 0.0	311 ± 12.0
SFNO	730 ± 0.0	730 ± 0.0	730 ± 0.0	730 ± 0.0	730 ± 0.0	730 ± 0.0	730 ± 0.0	730 ± 0.0	391 ± 108.3
AIFS	621 ± 73.2	502 ± 34.4	543 ± 33.5	649 ± 73.7	538 ± 30.6	576 ± 100.6	515 ± 33.2	622 ± 94.0	384 ± 24.1
GraphCast	295 ± 104.3	366 ± 146.7	730 ± 0.0	730 ± 0.0	586 ± 21.1	171 ± 21.1	450 ± 105.4	170 ± 5.6	125 ± 13.8
GenCast	98 ± 1.7	100 ± 3.6	106 ± 3.0	110 ± 4.5	98 ± 7.0	108 ± 5.1	99 ± 4.9	88 ± 4.2	84 ± 4.0

## C Noise injection in the rollout

### C.1 Adding Gaussian noise to the inputs

First, Gaussian noise is added to the inputs (surface and atmospheric variables), with a standard deviation equal to the standard deviation of the physical variable (Fig. A.6). This tests the model sensitivity to small-scale random perturbations.

Then, we explore more specifically Aurora sensitivity to different types of input perturbations. Figure A.9 shows Aurora denoising ability when surface and atmospheric variables are initialized with Gaussian random fields creating large-scale patterns (top) and a cat picture (bottom). In both cases, Aurora denoises the inputs within approximately 50 rollout steps and generates realistic rollout trajectories following seasonality.

Next, we decouple the influence of noise in static and dynamic (surface and atmospheric) variables. Figure A.10 shows Aurora rollouts initialized with static and/or dynamic variables set as random. Whenever static variables are the true physical ones, Aurora denoises the inputs, while input remain/become noisy when static variables are set as random.

### C.2 Initializing from pure noise

We initialize four models (Aurora, AIFS, SFNO, GraphCast) with pure white Gaussian noise,  $\mathcal{N}(\mu, \sigma^2)$ , when  $\mu$  (resp.  $\sigma$ ) is the mean (resp. standard deviation) of each physical variable.  $\mu$  and  $\sigma$  are scalar values and not two-dimensional fields to remove all their spatial content. Figure A.11 shows that each model performs a low-pass filtering of the noise. However, Aurora and SFNO denoise until realistic fields while AIFS and GraphCast show only unstructured noisy fields (Fig. A.12).

### C.3 Memorization in stable models

To test the memorization ability of stable models, we follow previous work [6, 13, 33] and say that a sample  $X_t$  is memorized if it is significantly closer to its first neighbor  $y_1(X_t)$  in the training dataset

$$y_1(X_t) = \arg \min_{X_\tau \in \mathcal{T}} \|X_t - X_\tau\|, \quad \mathcal{T} = \{\tau, |\text{doy}(\tau) - \text{doy}(t)| \leq 10 \text{ days}\} \quad (4)$$

than to its second neighbor  $y_2(X_t) := \arg \min_{X_\tau \in \mathcal{T} - \{y_1\}} \|X_t - X_\tau\|$ , as quantified by the distance ratio,

$$\frac{\|X_t - y_1(X_t)\|}{\|X_t - y_2(X_t)\|} \leq 0.5, \quad (5)$$

where doy is day of the year. Note that the set  $\mathcal{T}$  contains all days from the training period 1979-2019 that are within ten calendar days to the reference date  $t$  to avoid mixing different seasons. To reduce the computational costs of looking up the entire ERA5 dataset, three atmospheric levels (500, 850, 1000) are selected among the 13 used for training. Figure A.14 shows that the distance ratio is close to 1, indicating that no memorization is happening.

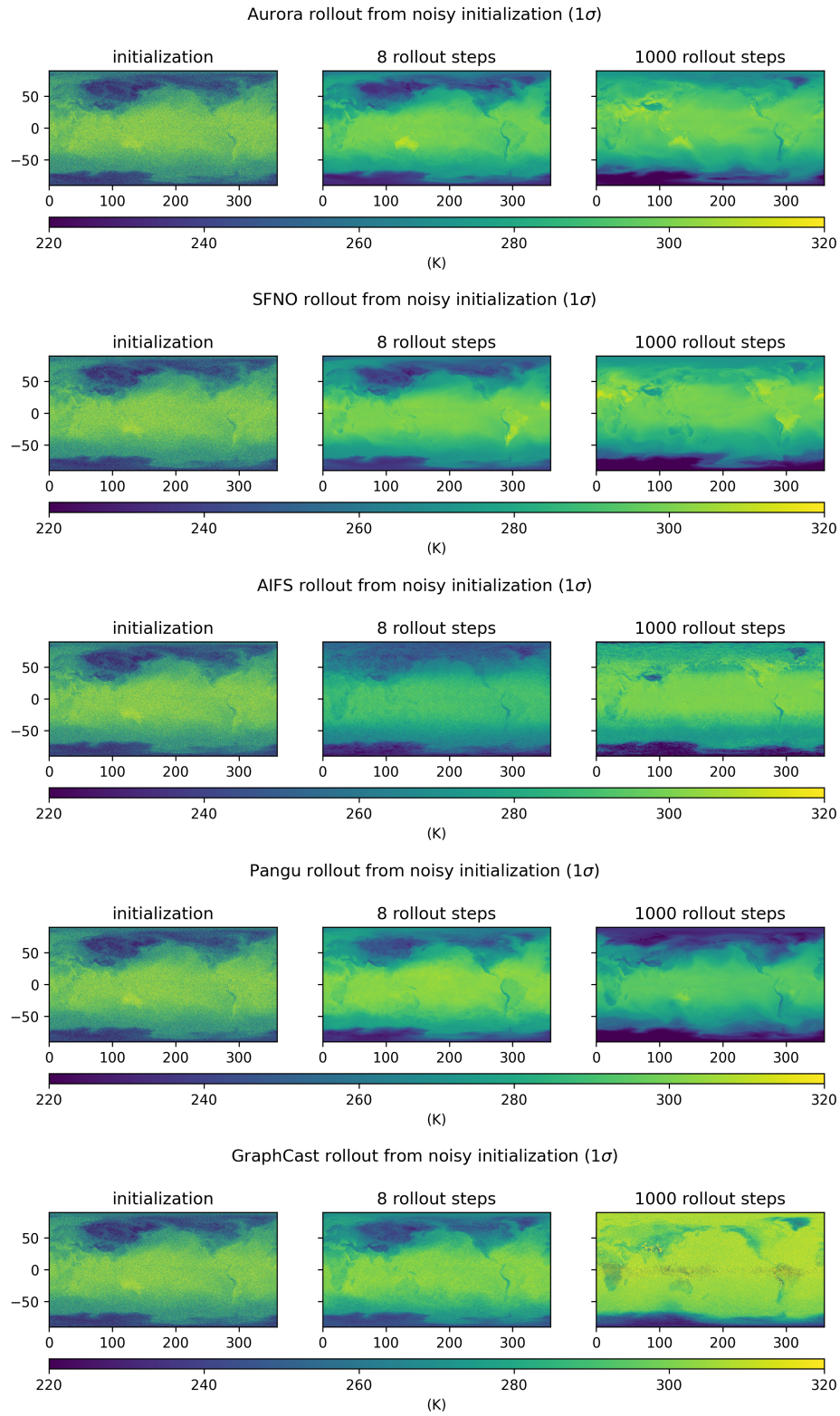


Figure A.6: 2-meter temperature at initialization (left), predicted after 8 (middle) and 1000 (right) rollout steps when inputs are perturbed with an additional noise of  $\sigma$

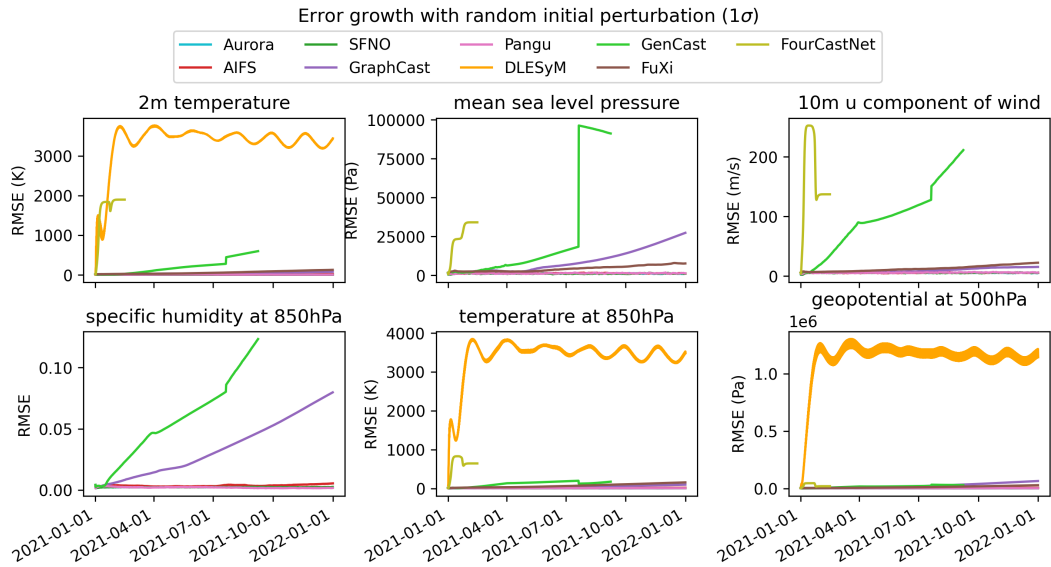


Figure A.7: Same as Fig. 2 but showing all models. Error between the reference rollout and the rollout initialised with a noisy input (additive noise with  $1\sigma$  standard deviation) for all models and six variables.

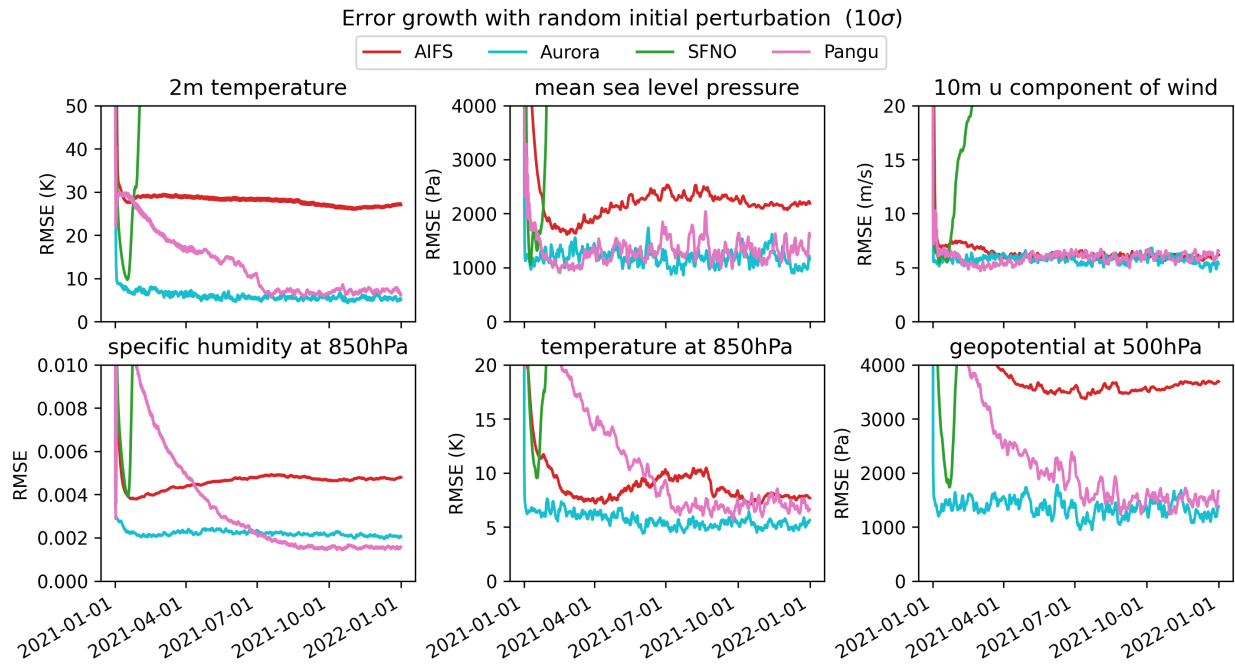


Figure A.8: Error between the reference rollout and the rollout initialised with a noisy input (additive noise with  $10\sigma$  standard deviation) for five models: Aurora (cyan), AIFS (red), SFNO (green), Pangu (pink) and six variables.

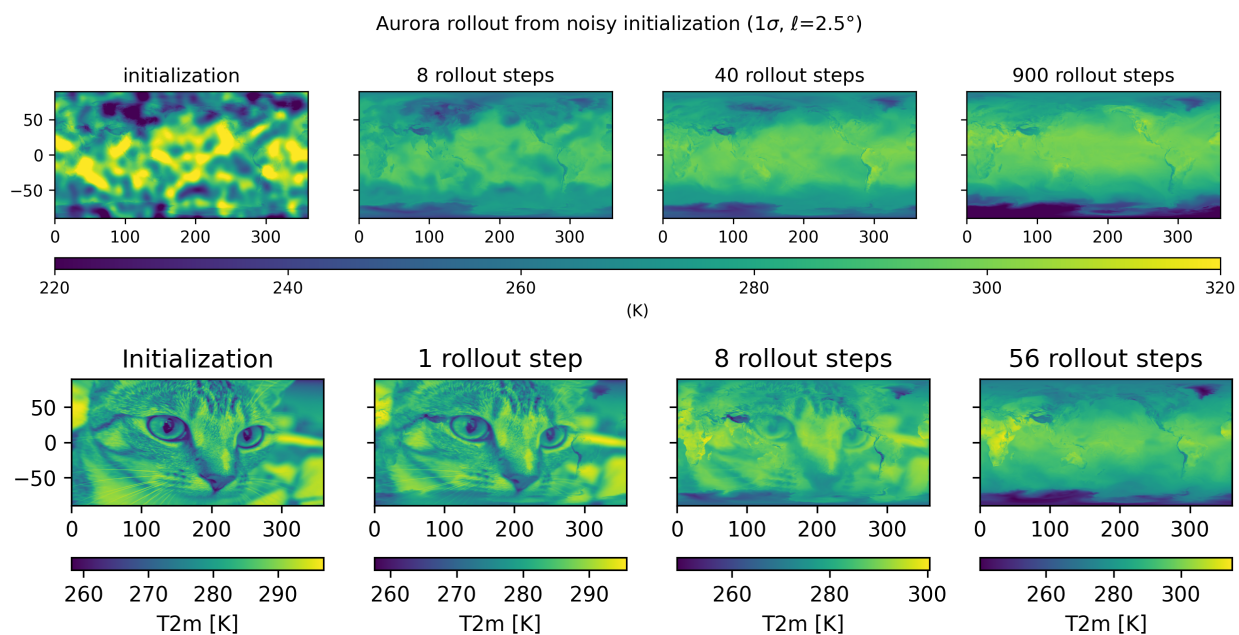


Figure A.9: 2-meter temperature predicted at different time stamps when (top) inputs are perturbed with an additive Gaussian random field with coefficient of variation  $\sigma^2$  (where  $\sigma$  is the standard deviation of the physical variable) and correlation length of 10 pixels (equivalent to  $2.5^\circ$ ), (bottom) surface and atmospheric variables are initialized with a cat picture.

### 2-meter temperature rollouts Aurora

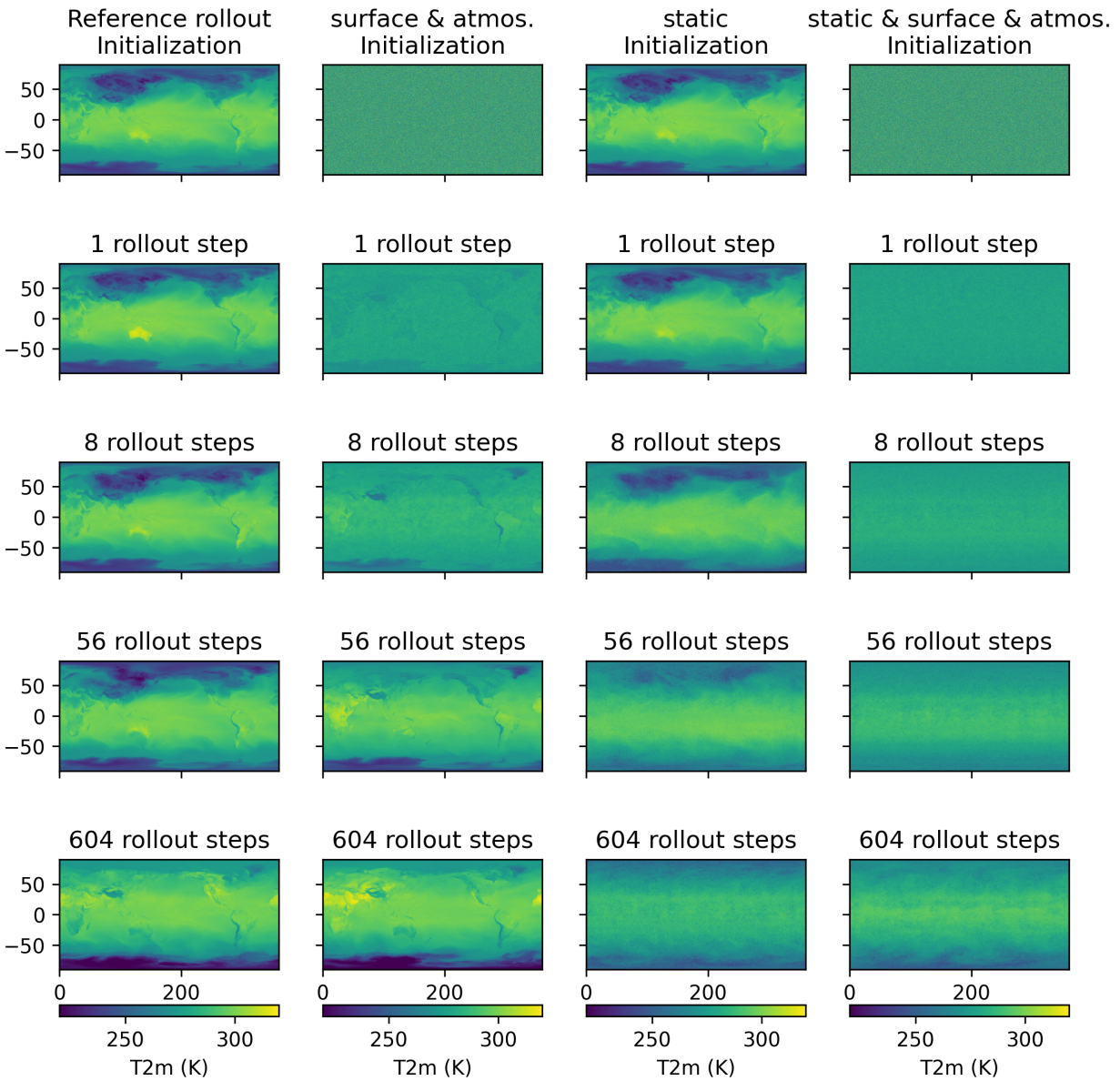


Figure A.10: 2-meter temperature predictions of four Aurora rollouts with different initialization, depicted at five rollout time steps. (1st column) Reference rollout. (2nd column) Initialize with random surface and atmospheric variables, static variables are left unchanged. (3rd column) Initialize with random static variables, surface and atmospheric variables are left unchanged. (4th column) Initialize with random static, surface, and atmospheric variables.

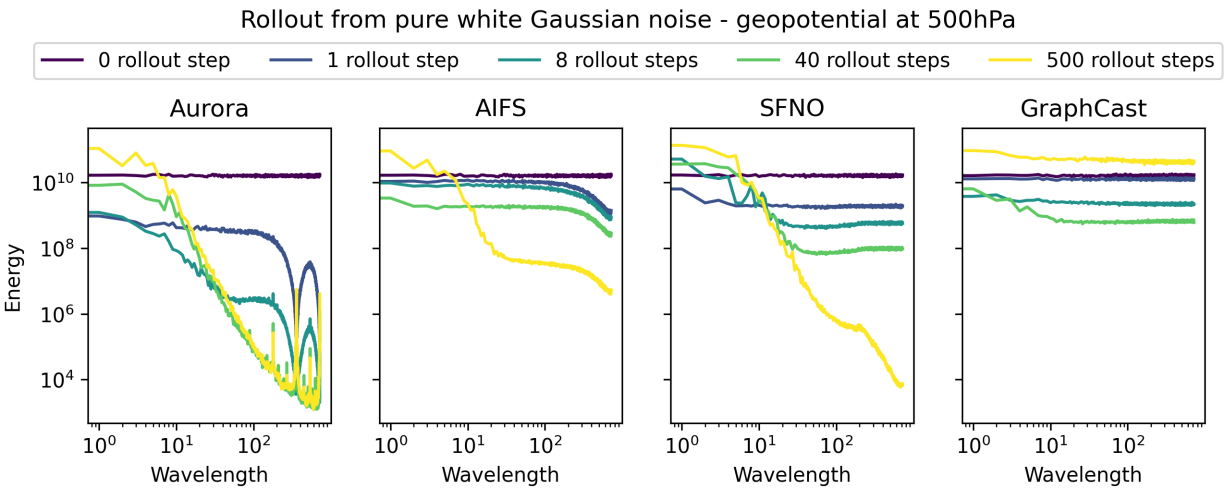


Figure A.11: Energy spectra of geopotential at 500hPa for four models (Aurora, AIFS, SFNO, GraphCast) at five iterations of the rollout when initialized from pure noise (colored lines).

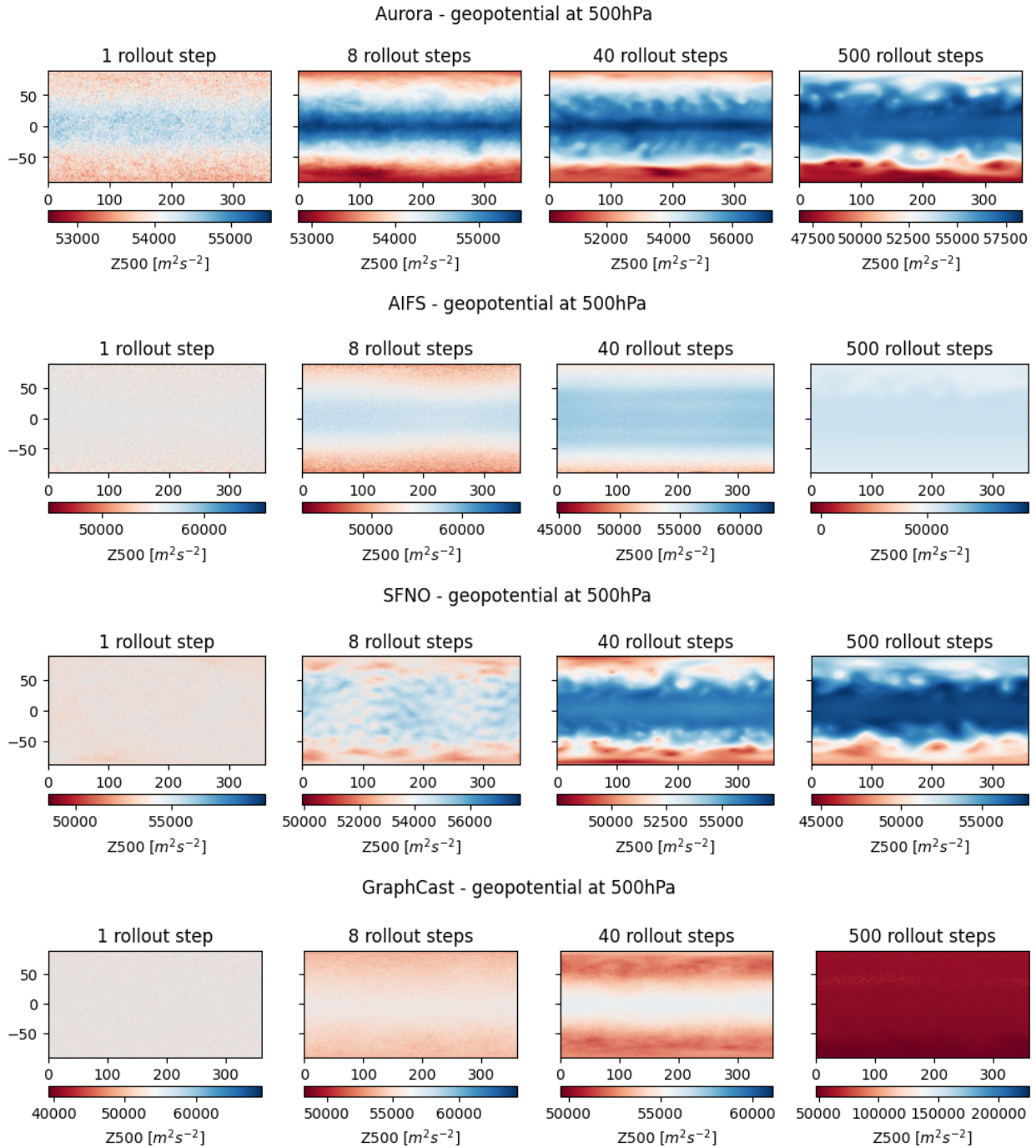


Figure A.12: Geopotential at 500hPa when the rollout is initialized with pure noise, depicted at four rollout iterations, for Aurora (first row), AIFS (second row), SFNO (third row), GraphCast (fourth row)

Spread between 5 rollouts from random initializations

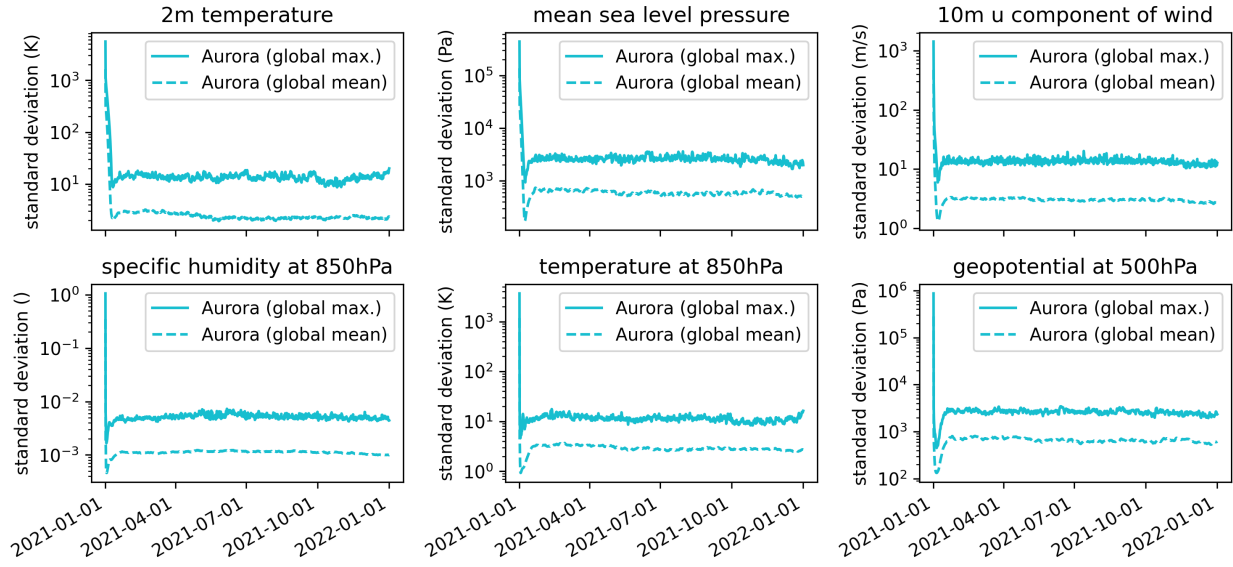


Figure A.13: Standard deviation across five Aurora rollouts initialized from pure white Gaussian noise. The plot shows the average of the standard deviation over all pixels (dashed line) and the maximum over the pixels (solid line). SFNO produces spread of the same order of magnitude.

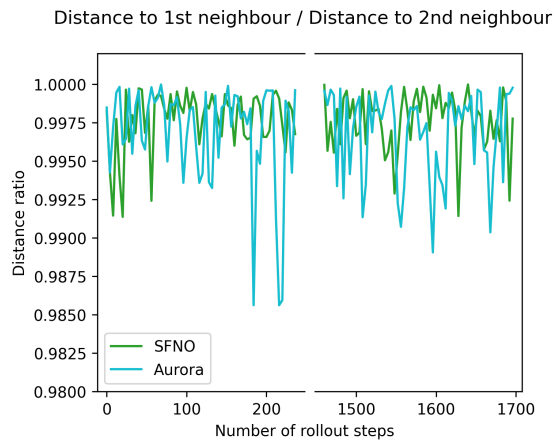


Figure A.14: Distance ratio between model predictions and ERA5, computed over all four surface variables, five atmospheric variables at levels 500 hPa, 850 hPa, 1000 hPa

## D Small Aurora models trained from random initialization

Aurora<sub>s</sub> is trained on 8 GH200 GPUs for 60k steps, with no gradient checkpointing and no model parallelism. The per-GPU batch size is 1, optimizer is AdamW, learning rate follows a linear warmup for 1k steps up to  $5e-4$  and the cosine decay. The training loss is latitude-weighted MAE with the same variabe-specific weights as [3]. Training time is between 13 hours ( $1.5^\circ$  resolution) and 22 hours ( $0.25^\circ$  resolution) due to the difference in data reading speed. The same batch size is used for all spatial resolutions for the sake of consistency between experiments but it could be increased for the lower resolution data.

Table A.4: Numbers of days before the loss of seasonality, for the four small Aurora models trained from scratch

Model	T2m	U10m	MSLP	Z500	T500	Q500	U300	T100	Q100
Aurora <sub>s</sub> , 6h, $0.25^\circ$	381	78	1450	> 1460	1451	211	399	> 1460	50
Aurora <sub>s</sub> , 24h, $0.25^\circ$	> 1460	> 1460	> 1460	> 1460	> 1460	244	> 1460	> 1460	> 1460
Aurora <sub>s</sub> , 6h, $1.5^\circ$	244	> 1460	> 1460	> 1460	635	> 1460	> 1460	> 1460	171
Aurora <sub>s</sub> , 24h, $1.5^\circ$	> 1460	> 1460	> 1460	> 1460	> 1460	> 1460	> 1460	> 1460	> 1460

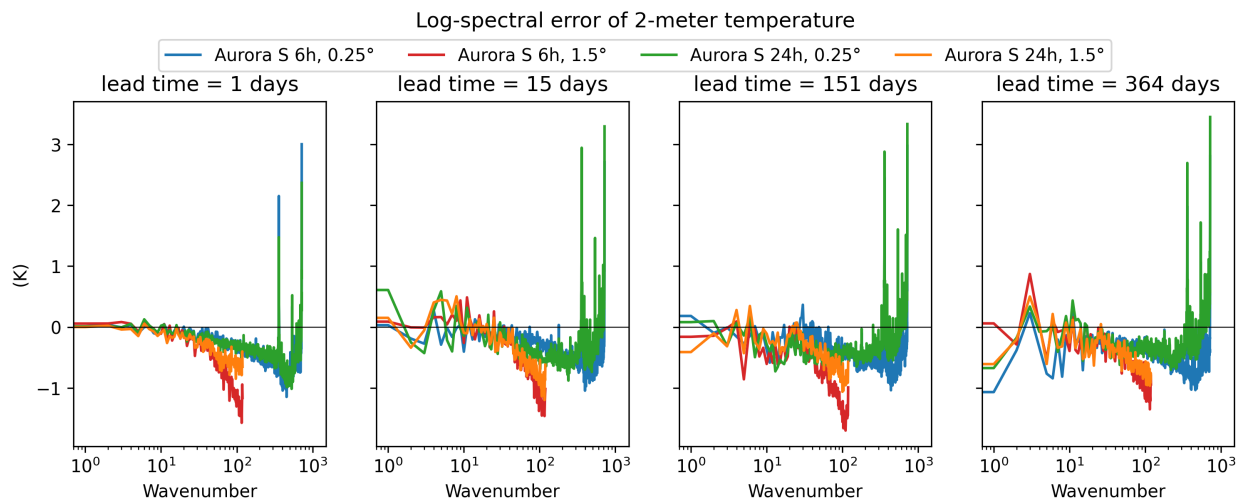


Figure A.15: Difference (in log scale) between the Fourier spectrum of the Aurora<sub>s</sub> models and the reference spectrum for ERA5, at different lead times

## E Climate extremes from rollouts

**Data and regions.** We analyze 2-meter temperature from ERA5 (0.25°, subsampled to 6-hourly). Five regions are selected: Central Europe (45–55°N, 5–20°E), Western US (30–50°N, 105–125°W), East Asia (25–45°N, 110–135°E), SE Australia (25–40°S, 140–155°E), and the Amazon (15°S–5°N, 45–70°W). At each 6-hourly timestep, we extract the regional spatial maximum and minimum of 2-meter temperature.

**Definition of extremes.** Thresholds are computed from the ERA5 climatological period 1990–2019: for each region, all temperature values (all pixels, all timesteps) are pooled and the 90th (P90) and 10th (P10) percentiles are computed. A *hot event* occurs when the regional spatial maximum exceeds P90; a *cold event* occurs when the regional spatial minimum falls below P10. Exceedance rates are evaluated over ERA5 2011–2020 and the Aurora rollout 2021–2031.

**Frequency analysis** We analyze the frequency of hot and cold events during the four-year time window for Aurora, SFNO, and DLESyM and compare it with ERA5. In this analysis, the threshold defining an extreme event is varied from the 80th to the 99.9th percentile for hot events (from 0.1st to 20th percentile for cold events). Results show that no model consistently reproduces extreme event frequency of ERA5 and no model is clearly better than the others (Fig. A.16). At the 90th percentile, the ratio of predicted hot events compared to ERA5 is between 0.7 and 1.1, with a clear tendency for ratios lower than 1.

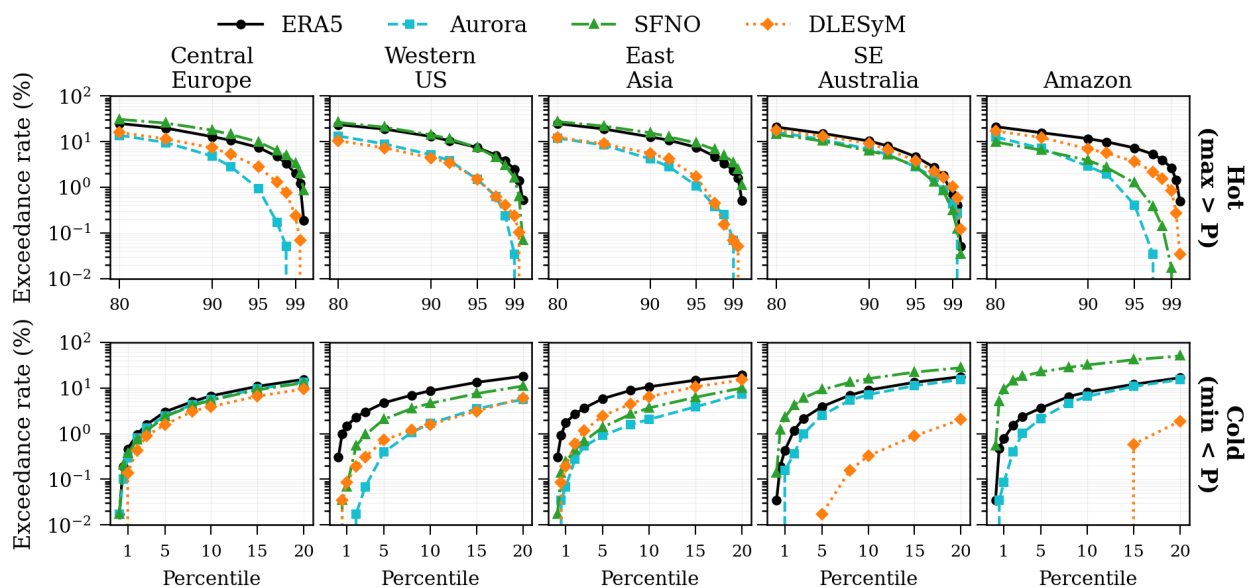


Figure A.16: Multi-threshold exceedance rates. For thresholds defined from the ERA5 distribution (P80–P99.9 for hot, P1–P20 for cold), the fraction of timesteps exceeding each threshold is shown. The growing gap at extreme thresholds indicates Aurora’s tails are lighter.

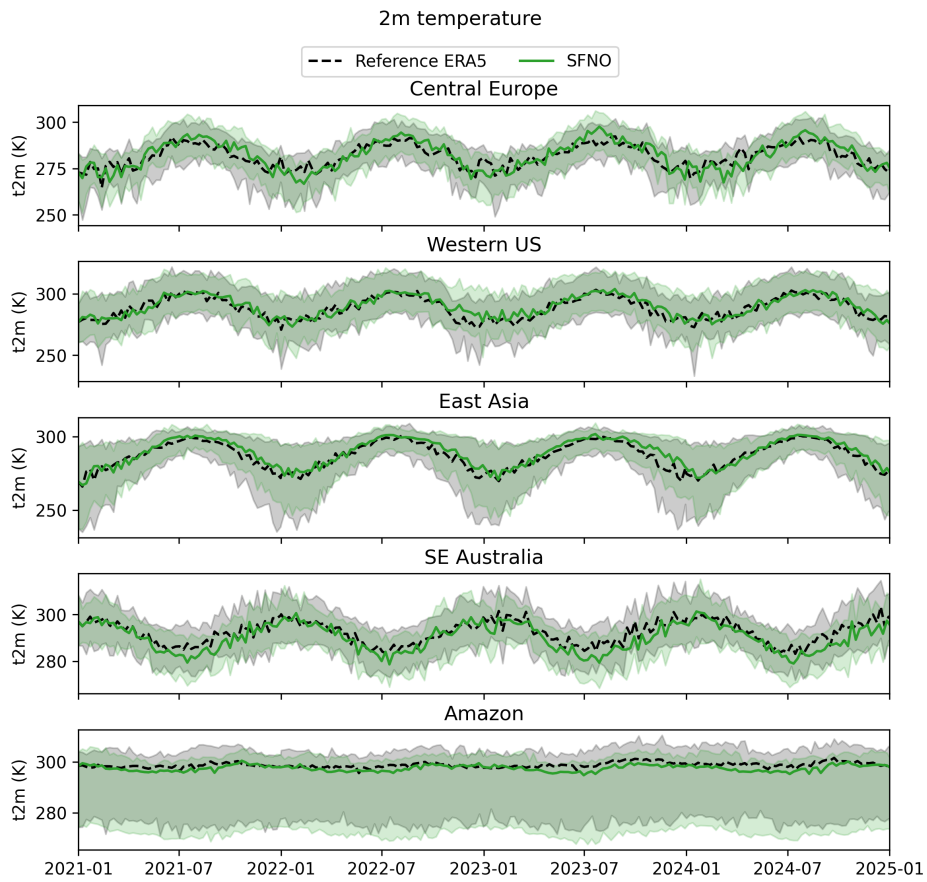


Figure A.17: 2-meter temperature in five regions for SFNO initialized on January 1st, 2021. The solid lines show the regional average, the shaded areas extend from the minimal to the maximal temperature over the region. The subplots show the first two months. Time series are depicted at a weekly resolution for easier visualization.